# Genome-wide crossover analysis in the holocentric pantry moth reveals strong crossover assurance and interference during spermatogenesis

LingSze Lee, Apratim Mitra, Leif Benner, et al.

*Genome Res.* 2026 36: 1574-1589 originally published online July 16, 2026
Access the most recent version at doi:10.1101/gr.281913.126

# Genome-wide crossover analysis in the holocentric pantry moth reveals strong crossover assurance and interference during spermatogenesis

LingSze Lee,[1] Apratim Mitra,[2] Leif Benner,[1] Melania Bruno,[3] Lorielle M. Raab,[1,4] Rose K. Runyan,[1] Emma Smith,[2] Ryan K. Dale,[2] and Leah F. Rosin[1]

[1]*Unit on Chromosome Dynamics, Division of Developmental Biology, Eunice Kennedy Shriver National Institute of Child Health and Human Development, National Institutes of Health, Bethesda, Maryland 20892, USA;* [2]*Bioinformatics and Scientific Programming Core, Eunice Kennedy Shriver National Institute of Child Health and Human Development, National Institutes of Health, Bethesda, Maryland 20892, USA;* [3]*Section on Mammalian Development and Evolution, Division of Developmental Biology, Eunice Kennedy Shriver National Institute of Child Health and Human Development, National Institutes of Health, Bethesda, Maryland 20892, USA;* [4]*Laboratory of Biochemistry and Genetics, National Institute of Diabetes and Digestive and Kidney Diseases, National Institutes of Health, Bethesda, Maryland 20892, USA*

Meiosis relies on programmed DNA double-strand breaks (DSBs) to initiate recombination between homologous chromosomes. Only a fraction of these breaks mature into crossovers (COs), creating the chiasmata essential for physically linking homologs and ensuring their accurate segregation in meiosis I. Errors in CO number or placement underlie a large fraction of human infertility and aneuploidies, yet how DSBs are designated to become COs and how the mechanisms ensuring COs form on all chromosomes (CO assurance) are not well understood, particularly in systems with a large number of chromosomes. Here, we investigate CO formation in the pantry moth, *Plodia interpunctella*, a novel invertebrate model system with $n = 31$ chromosomes. Using a combination of sequencing approaches, Oligopaints FISH, and statistical Weinstein tetrad analysis, we find robust CO assurance and interference in *Plodia*, with most chromosomes harboring only a single distal CO and few bivalents lacking COs. We employ CUT&RUN, ATAC-seq, and RNA-seq to profile the epigenomic landscape in *Plodia* testes, revealing that the distal chromosome arms in which COs form are enriched for heterochromatin and devoid of accessible chromatin, suggesting a bias for COs to form in repressed regions in the genome. These studies pave the way for future work diving deeper into the molecular regulation of CO formation in *Plodia* and other systems, in which the large number of chromosomes may be the key to revealing novel insights about CO regulation.

[Supplemental material is available for this article.]

Meiosis is the specialized cell division that occurs in the germline to produce haploid gametes. Once cells enter meiosis, maternal and paternal chromosome copies come together for pairing and meiotic recombination, also known as crossing over. In addition to generating genetic diversity, in most species, crossover (CO) formation also serves the key function of linking maternal and paternal homologs until they are segregated at anaphase I. This link between homologs not only prevents their premature separation but also is required for proper chromosome alignment and kinetochore tension at metaphase I (Nicklas 1997; Davis and Smith 2003; Nambiar et al. 2019). The accurate regulation of these chromosome dynamics during meiosis I is essential for the formation of healthy, viable gametes and failure to do so can result in chromosomal disorders or infertility (Bolcun-Filas and Handel 2018). In humans, many meiotic errors occur during these early stages of meiosis I as the result of defects in the number or placement of COs (Martin 2006; Sun et al. 2007a,b).

Crossing over begins with the formation of programmed DNA double-strand breaks (DSBs), a subset of which are repaired as COs (Gray and Cohen 2016). In most species, far more DNA DSBs form than COs (de Massy 2013), and most DSBs are repaired as non-CO events. How DSBs are designated into CO or non-CO repair is still a major question in the field. What is clear is that CO formation is very tightly regulated and governed by many "rules." First, CO assurance is a meiotic regulatory principle that ensures each homologous pair gets at least one CO to link them together (Darlington and Dark 1932; Owen 1949). Second, COs have a reduced likelihood of forming between adjacent regions of the same chromosome owing to CO interference (Sturtevant 1915; Muller 1916; Otto and Payseur 2019). Apart from yeast, systems with small chromosomes almost always have only one or two COs per chromosome owing to CO interference. Finally, COs are unlikely to form in chromosome regions required for genome stability, such as centromeres, which is known as the "centromere effect" (for review, see Saito and Colaiácovo 2017; Pazhayam et al. 2021).

Despite these widely observed rules, the factors that regulate CO formation and designation are highly diverse in sequence and function across species (Gerton and Hawley 2005; Kumar et al. 2010; Keeney et al. 2014; Dapper and Payseur 2019; Arter and Keeney 2024). As a result, CO locations vary across eukaryotes, even between closely related species (Price and Bantock 1975; Stapley et al. 2017; Samuk et al. 2020). The position and

**Corresponding author: leah.rosin@nih.gov**
Article published online before print. Article, supplemental material, and publication date are at https://www.genome.org/cgi/doi/10.1101/gr.281913.126. Freely available online through the *Genome Research* Open Access option.




36:1574–1589 Published by Cold Spring Harbor Laboratory Press; ISSN 1088-9051/26; www.genome.org

distribution of COs can even differ between individuals of the same species, such as differences in CO landscapes between males and females, called heterochiasmy (Lenormand and Dutheil 2005; Kong et al. 2014; Theodosiou et al. 2016; Brekke et al. 2023). Finally, CO placement can be altered owing to environmental factors such as temperature, infection status, and oxidative stress (Bomblies et al. 2015; Rybnikov et al. 2023).

The causes and consequences of this plasticity in CO formation are unclear, as are the mechanisms regulating CO assurance and interference. How does each cell ensure that all chromosomes get a CO? How does the formation of one CO prevent the formation of neighboring COs? Here, we employ the pantry moth, *Plodia interpunctella*, as a novel model system for interrogating CO formation. This study aims to broaden our analyses of meiotic recombination to include emerging systems such as *Plodia*, which is essential for revealing the true breadth of meiotic recombination strategies.

## Results

### Whole-genome sequencing of two laboratory strains of *Plodia* reveals genetic variation within and between strains

To analyze meiotic COs in *Plodia*, we obtained two divergent laboratory strains of *P. interpunctella*: the Savannah strain and the bFog strain (Fig. 1A). The Savannah strain originated as a wild strain isolated in Savannah, Georgia, and has been inbred in U.S. Department of Agriculture (USDA) laboratories since the late 1960s (Lum and Flaherty 1970). The bFog strain is a newer laboratory strain that was generated only a few years ago as a hybrid between two additional, independently isolated wild strains: the Dundee, United Kingdom, and the Florida laboratory strains (Heryanto et al. 2022). To map COs between chromosomes of these two strains, we first needed to identify all the genomic variants between these strains. For this, we performed whole-genome Illumina sequencing on three individuals per strain to generate genome-wide variant (SNP) maps. Because these are not isogenic strains and *Plodia* have not been inbred for as long as other laboratory systems like *Drosophila*, we were able to capture both interstrain variants and intrastrain variants using this approach.

Significant variation was observed both between the two strains and among the three individuals of each strain. Overall, the Savannah strain showed more intrastrain SNP variation than the bFog strain, with one Savannah individual being particularly different from the other two. We found this high variation within the Savannah strain quite surprising, because this strain has been inbred in laboratory cultures for >50 years. Among the three individuals per strain, the Savannah strain had more SNP variants on Chr 8 and 16, whereas bFog had more variants on Chr 6. Chr 7, along with the Z sex chromosome, had the smallest number of identified variants in both strains (Fig. 1B,C). These identified intrastrain variants (defined as any one individual harboring a distinct allele at that locus) were broadly distributed in clusters across chromosomes, with a few exceptions in which variants were more localized. For example, Savannah Chr 11 only had observed variants along one arm (we define "arms" as the distal thirds of a chromosome), and bFog Chr 2 and 9 harbored pockets of variants toward chromosome centers (Fig. 1C). In general, the identified bFog variants tended to be slightly closer to chromosome ends, whereas Savannah variants had less positional skew (Fig. 1D; Supplemental Fig. S1; Supplemental Table S1).

In agreement with the observed intrastrain SNP variation detected using Illumina sequencing, we also performed Pacific Biosciences (PacBio) long-read sequencing on three additional individuals per strain. Using the PacBio data, we identified many structural variants (insertions, deletions, or translocations) that were common to all three sequenced individuals of our Savannah stock compared with the reference *Plodia* genome generated from Savannah moths (Fig. 1E). However, it is worth noting that we did not perform Hi-C or other supplemental scaffolding approaches to verify this.

When comparing SNPs between the Savannah and bFog strains, we only considered alleles that were consistent between all three individuals of a strain and differed between strains. Using this method, we detected enough SNPs for accurate breakpoint detection in our data every 50–75 bp (Fig. 1F). To validate these strain-specific SNPs, we designed haplotype-specific Oligopaints (HOPs) (Beliveau et al. 2015; AlHaj Abed et al. 2019) for Chr 3 (Fig. 1G). These paints should exclusively label either the bFog Chr 3 or Savannah Chr 3 alleles, resulting in two nonoverlapping FISH signals for Chr 3 in hybrids. We tested these HOPs in cells with both paired and unpaired chromosomes in testes from first-generation ($F_1$) hybrids. We indeed observed two distinct FISH signals for Chr 3 (Fig. 1H–J). Notably, there are fewer variants toward the middle of Chr 3 for both strains (Fig. 1C,F, G), resulting in weaker FISH signals toward chromosome centers (in which there are fewer probes per kilobase). This is especially obvious when the chromosomes are in a linear configuration like at pachytene (Fig. 1I).

As a possible explanation for the genetic variation in our strains, we investigated repetitive DNA content in the *Plodia* genome. Repetitive sequences such as transposable elements (TEs) are often rapidly evolving owing to a lack of selective pressure at these loci (Finnegan 1989; Gbadegesin 2012; Lawlor and Ellison 2023). Using repeat modeling and annotation of the reference *Plodia* assembly, we identified several repetitive sequences likely belonging to TEs, which overall represent 18% of the *Plodia* genome (Supplemental Fig. S2A). Of all identified TEs, ∼9% are SINE-like, ∼30% are LINE-like, ∼15% are LTR-like, 6.5% are DNA transposons, and ∼40% are rolling circle (RC) repeats (Supplemental Fig. S2A). The relatively high representation of RCs, comprising ∼7% of the *Plodia* genome, is consistent with the broad range of RC abundances reported in Lepidoptera, in which considerable heterogeneity in RC content has been observed among species (Baril and Hayward 2022; Zhang et al. 2023; Perrier et al. 2025).

Repeat modeling performed on our strain-specific PacBio sequencing data also led to the identification of a potential satellite sequence with high sequence similarity between the bFog and Savannah strains, which is also present in the reference *Plodia* assembly (Supplemental Fig. S2B). Although this potential satellite sequence does not show any specific accumulation in chromosome arms versus centers, the majority of the TEs are found in the two distal arm regions of chromosomes genome-wide, except for small chromosomes in which TEs are more evenly distributed (Supplemental Figs. S3A, S4A; Supplemental Data Set S1).

We tested whether strain-specific variants are enriched within these TEs, and we found that, indeed, variants are significantly enriched in TEs, but the odds ratios are low (1.2 for Savannah and 1.18 for bFog, Fisher's exact test). (Supplemental Fig. S3A,B; Supplemental Data Set S2; Supplemental File S1). If variants are more likely to accumulate in repetitive elements, then perhaps they are excluded from coding regions like gene bodies. When we tested whether variants are excluded from gene bodies or not,

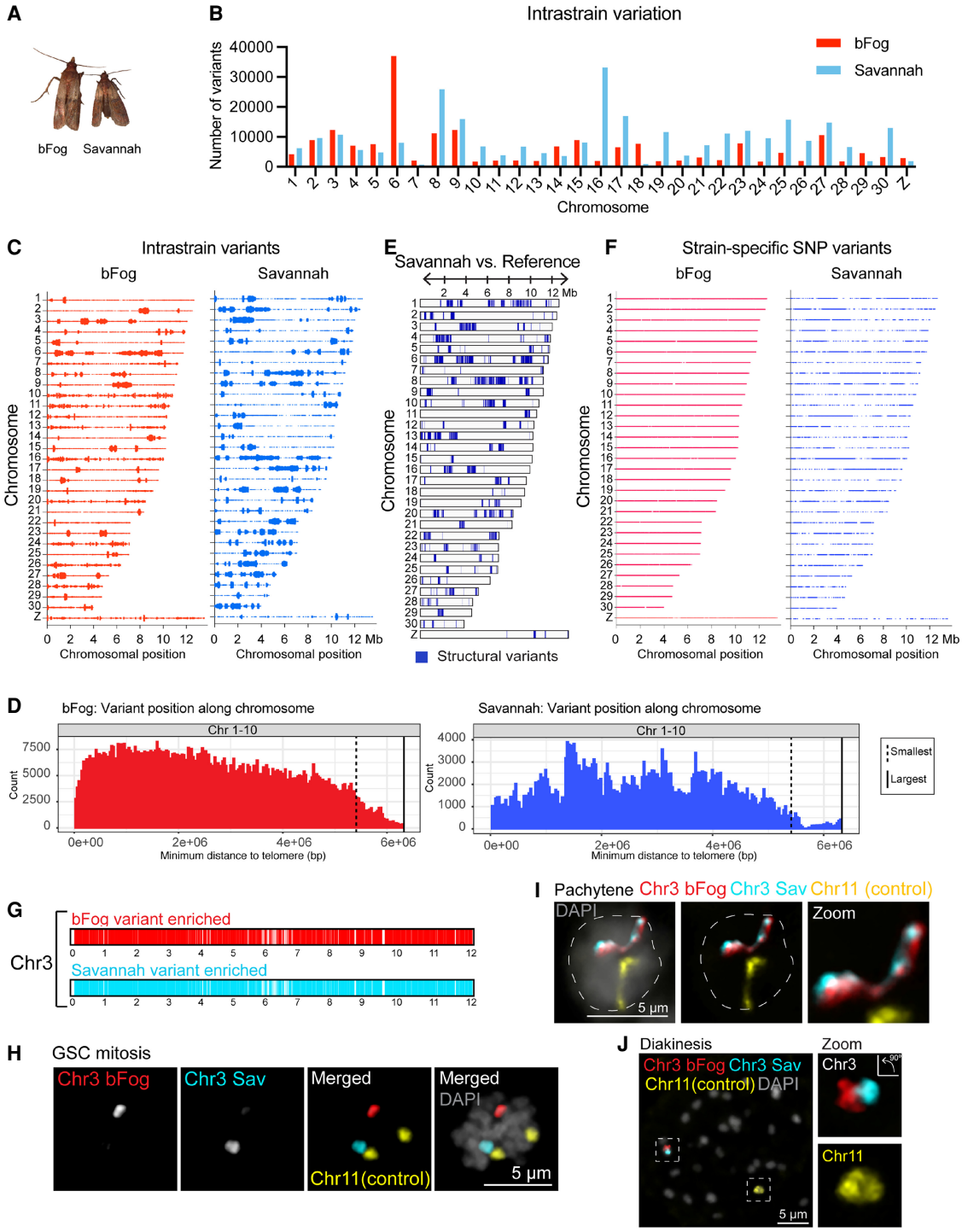


**Figure 1.** Genetic variation in *Plodia* strains. (*A*) Image of the adult female *Plodia interpunctella* strains used in this study: the bFog strain (*left*) and the Savannah strain (*right*). (*B*) Number of variants per chromosome between individuals in our bFog (red) and Savannah (blue) strains. The plot shows the count of variants across three WT individuals for each strain. An intrastrain variant is a single–base pair locus that is different between any of the individuals. (*C*) Plots showing the position and enrichment of intrastrain variants on individual chromosomes for the bFog strain (*left*) and Savannah strain (*right*). (*D*) Histogram showing the minimum distance of identified strain-specific variants from the end of a chromosome, in which the number of variants for each chromosome is binned using 30 kb windows. The genome was subdivided into three chromosome-sized groups, with Chr 1–10 (largest; 12.65–10.82 Mb) shown here. The "skewness" of variants toward the chromosome end is as follows for Chr 1–10: Savannah = 0.157 and bFog = 0.276. Dashed lines show the mid-point of the smallest chromosome per chromosome group, and solid lines show the mid-point of the largest chromosome per chromosome group. (*E*) Representative structural variants (blue) detected in the genome of our Savannah strain individuals compared with the reference *Plodia* Savannah genome. (*F*) Haplotype-specific variants per chromosome in the bFog (red) and Savannah (blue) strains. (*G*) Schematic of HOPs for Chr 3 designed based on variants detected in the whole-genome sequencing data. (*H–J*) Chr 3 HOPs FISH on mitotic germline stem cell (*H*), pachytene cell (*I*), and diakinesis cell (*J*) from male $F_1$ hybrids testes squashes. DAPI is shown in gray, bFog Chr 3 in red, Savannah (Sav) Chr 3 in blue, and Chr 11 control in yellow.

we found that, yes, both of the Savannah and bFog variants are significantly depleted from gene bodies but, again, with mild odds ratios (0.86 and 0.92, respectively). In summary, variants are somewhat enriched in TEs and excluded from gene bodies, but the biological significance of this is unclear. Regardless of the underlying mechanism, the variations we detected using this genome sequencing approach suggest that the *Plodia* genome is not necessarily under strong purifying selection and may even have regions that are quickly evolving.

## CO analysis in *Plodia* reveals strong CO assurance and interference

Having identified genome-wide, strain-specific variants in our wild-type parental strains (WTs), we needed to generate hybrids to map COs. As only male meiosis is reported to involve COs in Lepidoptera (Rasmussen 1977; Rasmussen and Holm 1982; Xiang et al. 2024), we isolated hybrid males ($F_1$s) which harbor sperm containing CO chromatids. We then crossed these male $F_1$ hybrids back to either WT Savannah or WT bFog females to generate $F_2$ hybrids heterozygous for $F_1$ COs (Fig. 2A). Whole-genome sequencing was performed on these $F_2$s. A detailed description of these crosses can be found in the Methods. As a control, we also generated $F_2$s from $F_1$ hybrid females backcrossed to WT Savannah males ("HFS"), from which we expected to recover no $F_1$ COs (Supplemental Fig. S5A,B).

From the genomic DNA of these $F_2$ hybrids, we performed Illumina sequencing, computationally identified strain-specific variants, and performed downstream analysis to detect $F_1$ COs (see Methods). Variants were called relative to the Savannah strain reference genome. Because of the expected greater number of variants from the bFog background, we used different quantification methods for hybrids backcrossed to WT bFog versus WT Savannah. For $F_2$s derived from backcrosses to WT Savannah females ("HS"), the presence of bFog-specific variants indicated $F_1$ CO, as visualized by coverage plots (Fig. 2B; Supplemental Fig. S5C). For $F_2$s derived from backcrosses to WT bFog females ("HB"), the above approach did not work as the resultant plots were too sparse (Supplemental Fig. S5D). Thus, for the "HB" $F_2$ hybrids, we devised an alternate variant classification strategy that utilized the transition from heterozygosity to homozygosity for bFog variants as an indication of an $F_1$ CO, as visualized by variant plots (Supplemental Fig. S6A,B). Consistent with previous reports of achiasmatic female meiosis, $F_1$ female backcrosses revealed no COs in the $F_2$s (Supplemental Fig. S5B). As negative controls, we also analyzed WT Savannah and WT bFog genomes with this pipeline. WT Savannah genomes showed no bFog variants, and WT bFog genomes had bFog variants throughout the entire genome (Supplemental Fig. S5E).

Using the coverage plots and variant plots, we then manually quantified the number and location of COs for all 30 autosomes from 73 $F_2$s, totaling 2190 chromosomes (Supplemental Table S2). We excluded the Z Chromosome from these analyses owing to a lack of variants on the Z Chromosome, which made it difficult to precisely map COs (Supplemental Fig. S6A). No CO (NoCO), single CO (SCO), and double CO (DCO) chromatids were all present in the $F_2$ population (Fig. 2B,C; Supplemental Figs. S5C, S6A,B). Genome-wide, 47% of $F_2$s chromatids were NoCOs ($n = 1025$), 50% were SCOs ($n = 1096$), and 3% were DCOs ($n = 69$) (Fig. 2C). To corroborate the sequencing data, we also quantified COs on Chr 3 using the HOPs probes on haploid round spermatids from $F_1$ hybrid males ($n = 668$ cells). This revealed a very similar ratio of NoCOs (37%), SCOs (50%), and DCOs (13%) for Chr 3 compared with the $F_2$ sequencing data (Fig. 2D,E). No triple COs were observed using either method, but it is still possible that they occur and are too rare for us to have observed in these analyses. Based on the $F_2$ sequencing data, the genome-wide average recombination rate for *Plodia* was calculated to be 6.58 cM/Mb, with individual chromosomes ranging from 3.9 to 14.5 cM/Mb (Supplemental Table S2). This is similar to a recent study in the white wood butterfly, which reported a genome-wide recombination rate of 7.37 cM/Mb and a chromosomal range of 3.5–15.3 cM/Mb (Torres et al. 2023).

To analyze levels of CO interference, we calculated the genome-wide coefficient of coincidence (CoC) for COs from our $F_2$s, which considers the frequency of observed versus expected DCOs to predict CO interference (Sturtevant 1915; Muller 1916; Chuang and Smith 2023). A CoC of zero indicates complete CO interference, and a CoC of one indicates no interference. Similar to previous observations in *Drosophila* (Foss et al. 1993) and most other systems (Chuang and Smith 2023), we find that in *Plodia* CO interference is strongest over short genetic distances (low CoCs), and interference decreases as genetic distance increases (CoCs rise) (Fig. 2F). However, unlike *Drosophila*, which shows a relatively consistent decrease in interference as genetic distance increases, we find that *Plodia* still shows high interference (low CoC values) until at least 60 cM of genetic distance (Fig. 2F), suggesting stronger interference over larger genetic distances in *Plodia* than in *Drosophila*.

Using our sequencing-based quantification of COs present in $F_2$s (Fig. 2C), which represents the chromatids inherited from $F_1$s and not directly the number of COs that formed in $F_1$ meiosis, we performed Weinstein tetrad analysis to estimate the number of COs that occurred in tetrads during $F_1$ spermatogenesis. Weinstein tetrad analysis is a maximum-likelihood approach used to calculate the expected frequency of different types of tetrads/bivalents (NoCO, SCO, DCO, etc.) produced by a single meiosis when only one of the four meiotic products is observed/inherited (Weinstein 1936, 1958). For example, a tetrad with one CO (SCO) during $F_1$ meiosis I will lead to the observation of two NoCO and two SCO $F_2$ progeny (Supplemental Fig. S7D). Genome-wide Weinstein tetrad analysis suggests that ~5% of $F_1$ tetrads lacked COs (NoCOs; 95% CI [4.14, 6.54]), 81% had SCOs (95% CI [78.22, 83.77]), and 14% had DCOs (95% CI [10.99, 16.33]) (Supplemental Fig. S7E). This low prevalence of NoCO tetrads predicted by the Weinstein analysis indicates strong CO assurance, and the low prevalence of DCO tetrads suggests strong CO interference. These Weinstein estimates are consistent with imaging-based analysis of prophase I COs in *Plodia* using a custom HEI10 antibody (Fig. 2G,H; Supplemental Fig. S7F), which demonstrated that the majority of late pachytene nuclei harbor about 30 HEI10 foci (about one CO per bivalent), but variations in the number of foci are also present, ranging from 20 to 40 foci per nucleus. Overall, our CO data support a model in which *Plodia* has strong CO assurance and interference genome-wide.

## CO patterning differs from chromosome to chromosome in *Plodia*

Studies in both plants and animals have shown that chromosome size can greatly impact CO patterning. For example, across kingdoms, COs tend to accumulate near chromosome ends, and small chromosomes typically form fewer COs compared with large chromosomes (Haenel et al. 2018; Wang et al. 2021). Thus, we wanted to investigate the connection between chromosome size and CO patterning in *Plodia*. To this end, we plotted chromosome size versus DCO frequency based on our $F_2$ data (Fig. 3A,B). In *Plodia*,

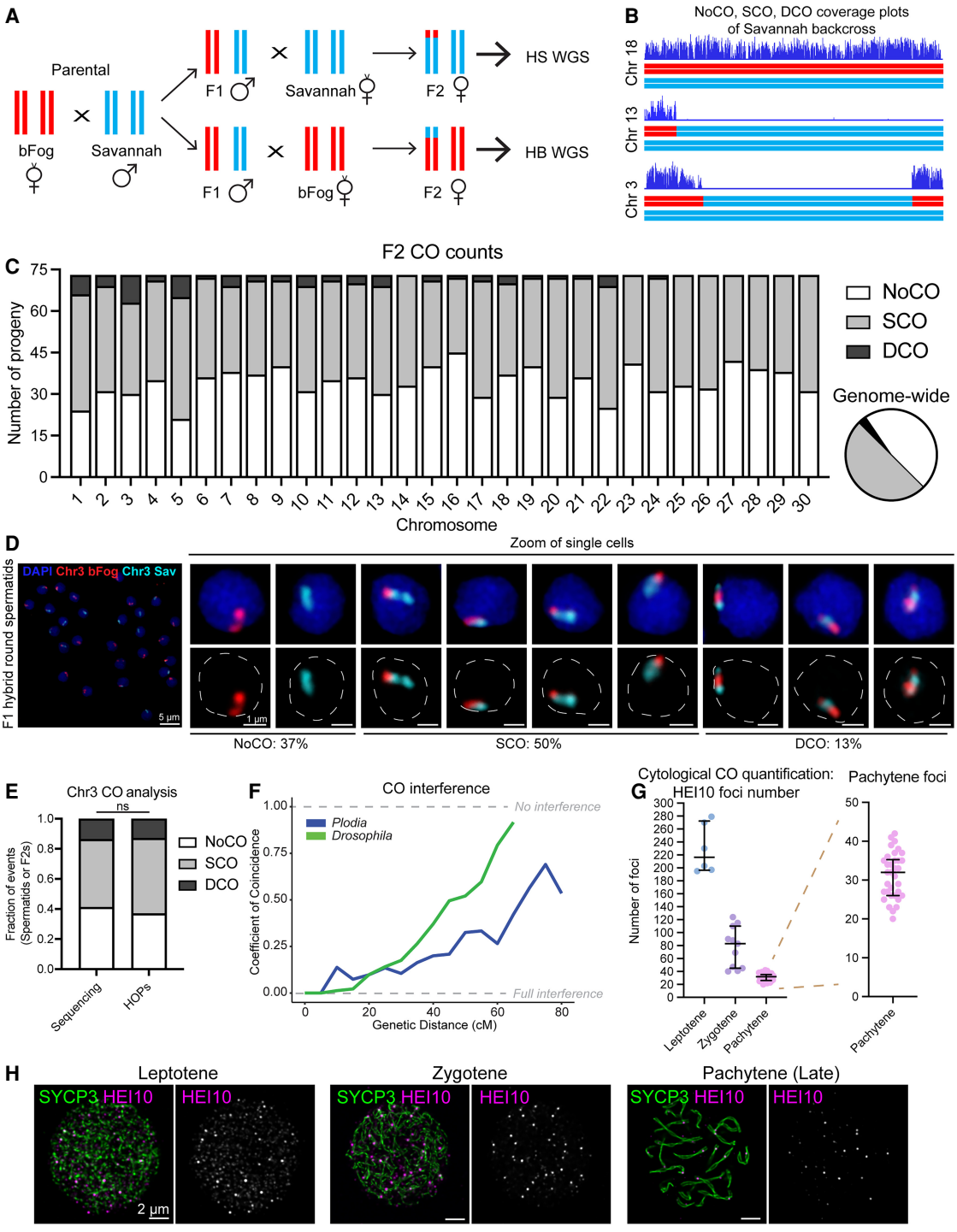


**Figure 2.** CO analysis in *Plodia*. (*A*) Schematic of crosses to generate hybrids for whole-genome sequencing. bFog chromosome is shown in red and Savannah chromosome in blue. (*B*) Representative coverage plots of Savannah backcrosses for three chromosomes to visualize CO(s). SNP coverage plots for Chr 18, 13, and 3 showing NoCO, SCO, and DCO, respectively. (*Top*) SNP density plot and (*bottom*) chromatids for each chromosome after CO showing chromosome regions from bFog (red) and Savannah (blue), as shown in *A*. (*C*) Bar graph showing $F_2$ CO quantification in this study for each chromosomal location of CO chromatids identified in the $F_2$s. NoCO is shown in white, SCO in gray, and DCO in black. (*Bottom right*) Pie chart showing genome-wide percentage of COs quantified in $F_2$ hybrids. NoCO = 47%, SCO = 50%, and DCO = 3%. (*D*) Round spermatids labeled with HOPs, with the Savannah allele in cyan and the bFog allele in red. DAPI is shown in blue. (*Left*) Field of cells; (*right*) zoom of representative single cells showing NoCO, SCO, or DCO; and (*below*) quantification percentage for Chr 3 in round spermatids. (*E*) Quantification of COs present on Chr 3 in round spermatids by FISH compared with $F_2$ sequencing. (*F*) Coefficient of coincidence (CoC; observed/expected DCO events) versus genetic distance for both *Plodia* (blue) and *Drosophila* (green). A CoC value of one indicates no CO interference. (*G*) Quantification of HEI10 foci number based on immunofluorescence in early prophase I cells from spermatocyte spreads. (*Right*) Zoom of HEI10 quantification at pachytene. (*H*) Representative images of HEI10 immunofluorescence in early prophase I cells (leptotene, zygotene, and pachytene).

chromosome name/number is inversely related to chromosome size, in which Chr 1 is the largest autosome and Chr 30 is the smallest (Fig. 1C,E,F; Supplemental Table S2). We found that, indeed, there is a mild correlation between chromosome size and the number of DCOs, with larger chromosomes being generally more likely to harbor DCOs compared with small chromosomes (Figs. 2C, 3A,B; Supplemental Fig. S7A). However, some chromosomes are more likely to harbor DCOs than others of a similar size, as revealed by them being outliers on the chromosome size versus DCO plot (Fig. 3A,B; Supplemental Fig. S7A). For example, although Chr 1–6 are all ∼12 Mb in length, DCOs on Chr 3 were observed in 14% of individuals, DCOs on Chr 5 were observed in 11% of individuals, and DCOs on Chr 1 were observed in 10% of individuals. Conversely, Chr 2, 4, and 6 only had observed DCOs in 5%, 3%, and 1%, respectively, of individuals (Figs. 2C, 3A). Similarly, Chr 22–25 are all 7 Mb in length, and only Chr 22 had a >1% DCO rate (5%) (Figs. 2C, 3A,B). Similar deviations for these chromosomes were observed using chromosome-specific Weinstein estimates based on the $F_2$ sequencing data (Supplemental Fig. S7G). Importantly, Weinstein estimates for Chr 3 based on the HOPs probes quantification similarly suggest that there might be a large fraction of DCOs on Chr 3 (Supplemental Fig. S8C). In agreement with some chromosomes being more biased to DCOs than others, those chromosomes with higher frequencies of DCOs have a longer genetic distance than other chromosomes of a similar physical distance (Fig. 3C).

In addition to possible chromosome-specific biases in DCO formation, we also found that COs are not randomly distributed along the chromosome length in *Plodia*. For all chromosomes, we found that COs in our sequencing data are significantly skewed toward chromosome arms (the outer-most third of the chromosome), with this bias being most pronounced for larger chromosomes (Fig. 3D; Supplemental Fig. S7B,C; Supplemental Table S3). However, when we plotted CO position as a normalized distance from the nearest telomere for large, medium, or small chromosomes, we observed similar distributions regardless of chromosome size (Fig. 3D), in which COs are most likely to form ∼1–2.5 Mb (median = 1.5 Mb) from the telomere and not at a specific position on the chromosome (arm vs. center). This is similar to data from both plants and animals, including the roundworm *Caenorhabditis elegans* in which COs form ∼0.6–1 Mb from the chromosome ends (Saito and Colaiácovo 2017; Haenel et al. 2018; Castellani et al. 2024). When DCOs form on long chromosomes, these two COs are even more distal than SCOs on the same chromosomes, with DCOs forming only 0.5–2 Mb (median = 1 Mb) from the telomere (Fig. 3E), further supporting the presence of strong CO interference in *Plodia*.

## COs are not enriched in gene bodies, GC-rich regions, or TEs

In *C. elegans*, the distal chromosome arms in which COs tend to form are more gene-poor compared with chromosome centers. However, in *Plodia* and most moths, genes are more uniformly distributed across chromosomes (Supplemental Fig. S9; Rosin et al. 2021; Hockens et al. 2024). Still, we wondered whether it is still possible for COs to be depleted from genes on the chromosome arms. Using Fisher's exact tests followed by multiple testing adjustments with our $F_2$ sequencing data, we find that COs are, in general, mildly depleted from gene bodies (adjusted *P*-value = 0.007, odds ratio = 0.84). Of those COs that were found in genes, they are significantly more likely to be in introns than in exons (adjusted *P*-value = $2.11 \times 10^{-7}$, odds ratio = 1.69), and COs are significantly depleted from promoters defined as transcript-level transcription start sites (TSSs) ±500 bp (adjusted *P*-value = $4.7 \times 10^{-5}$, odds ratio = 0.6). Among COs that do fall within genes, the genes on chromosome arms are actually enriched for COs compared with those in the middle of the chromosome (adjusted *P*-value = $1.1 \times 10^{-15}$, odds ratio = 1.89). Together, this means COs tend to be less common in genes throughout the genome, but they still occur in genes located on chromosome arms rather than being excluded from them.

Similarly, GC-rich chromatin has been associated with meiotic CO formation in both plants and animals and is often associated with open/active chromatin domains (Eyre-Walker 1993; Glémin et al. 2014; Rodgers-Melnick et al. 2015; Hinch et al. 2019). In *Plodia*, we find that GC content is relatively even across chromosomes apart from the AT-rich telomeric repeats (Supplemental Fig. S10; Okazaki et al. 1993; Vítková et al. 2005). We find no significant correlation between GC content and CO position (Pearson's correlations over 1 kb windows range from −0.01 to 0.01, depending on the chromosome).

Because COs are not enriched in gene bodies or GC-rich domains, we wondered if they might be enriched in TEs, which we showed above are also enriched in chromosome arms (Supplemental Fig. S4; Supplemental Data Set S1). To test this, we calculated the observed occurrence of COs in TEs and compared it to the expected occurrence by chance (Supplemental Data Set S3). Although some COs do fall within TEs and other repeats, we did not observe a significant enrichment of COs in TEs or any other repetitive sequences (adjusted *P*-value = 0.27, odds ratio = 1.09) (Supplemental Data Set S3; Supplemental File S1). Importantly, we also did not see a correlation between COs and variants in either strain, with Pearson's correlations over 1 kb windows being between −0.014 and 0.038 for Savannah-specific variants and −0.0047 and 0.035 for bFog-specific variants. Thus, COs are not enriched in TEs and are not significantly associated with genetic variants in either strain.

## COs are more likely to occur in heterochromatic chromosome regions

Because we did not observe an enrichment of COs in TEs, genes, or GC-rich chromatin, we wondered what makes chromosome arms a more hospitable environment for CO formation in *Plodia*. To this end, we generated the first comprehensive chromatin landscape map for *Plodia* testes by performing CUT&RUN, ATAC-seq, and RNA-seq to map histone modifications, chromatin accessibility, and transcription, respectively (Fig. 4A; Supplemental Fig. S12). This was done in whole larval testes, in which a large fraction of cells are in meiotic prophase I (Supplemental Fig. S11A,B; Buenrostro et al. 2015; Skene and Henikoff 2017; Rosin et al. 2021).

CUT&RUN was used to map the following histone modifications: H3K4me1, H3K4me3, H3K9me2, H3K9me3, H3K27me3, H3K36me3, H3K27ac, H4K16ac, H4K20me1, H3.3, and RNA polymerase II CTD ser5 phosphorylation (Pol II Ser5P) (Fig. 4A,B). Using these data, we then trained hidden Markov models with ChromHMM to segment the genome into different nonoverlapping chromatin states in larval testes and determine if COs are enriched within any specific state (Ernst and Kellis 2012). After manual inspection of models built with up to 15 states, we selected the eight-state model for its interpretability. Based on the histone marks associated with each state, as well as the enrichment of certain genomic features within the states, such as annotated gene introns/exons or TSSs, we classified each of the eight states as follows

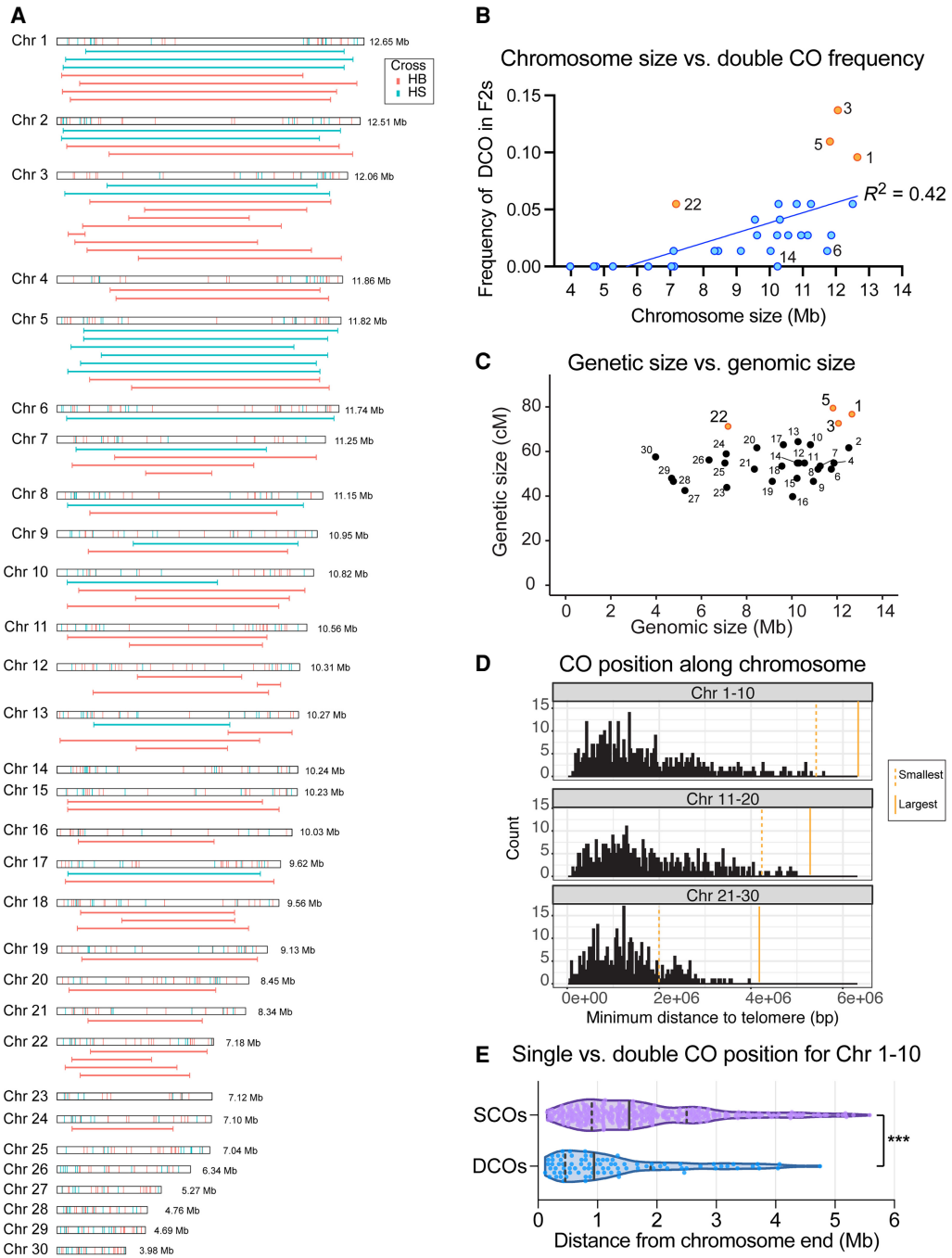


**Figure 3.** CO distribution in *Plodia*. (*A*) CO positions for $F_2$ progeny, in which each chromosome is shown separately. Observed SCOs are shown at the *top* in the chromosome-scale box, and DCOs (when observed) are shown *below*. Each end of a horizontal line represents the position of one of the two COs in a DCO chromatid. COs from WT Savannah backcrosses are shown in blue, and COs from WT bFog backcrosses are shown in red. (*B*) Scatter plot showing correlation analysis for chromosome size (*x*-axis) versus DCO frequency (*y*-axis) from the $F_2$ hybrids. A single blue or orange dot represents each chromosome. Orange dots are outliers *above* the line of best fit. Linear regression was used to calculate the line of best fit, $R^2$. (*C*) Scatter plot showing physical genomic size of individual chromosomes (*x*-axis) versus genetic size in centimorgan calculated based on $F_2$ data (*y*-axis). Orange dots are the outliers from *B*. (*D*) Histogram showing the minimum distance of a CO from the end of a chromosome, in which the number of COs for each chromosome are binned using 30 kb windows. The genome was subdivided into three chromosome-sized groups, with Chr 1–10 (largest; 12.65–10.82 Mb) shown at the *top*, Chr 11–20 (10.56–8.45 Mb) shown in the *middle*, and Chr 21–30 (smallest; 8.34–3.98 Mb) shown at the *bottom*. Dashed orange lines show the mid-point of the smallest chromosome per chromosome group, and solid orange lines show the mid-point of the largest chromosome per chromosome group. (*E*) Violin plots comparing CO position relative to chromosome end for SCO and DCO on Chr 1–10. Each dot represents one CO. Solid lines represent the median. Dashed lines represent the upper and lower quartiles. $P = 0.0004$, Welch's *t*-test.

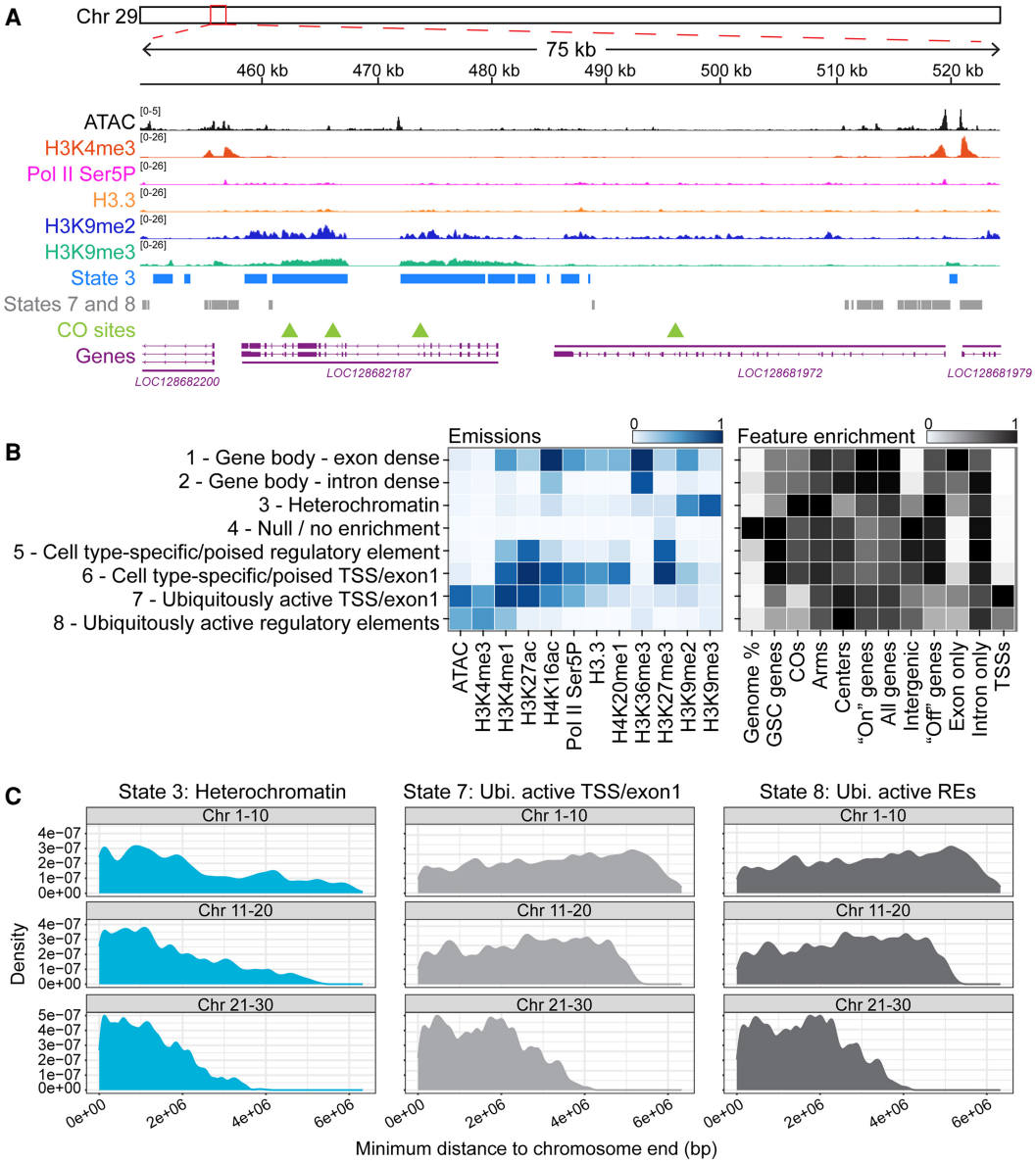


**Figure 4.** COs occur in heterochromatic regions of the genome in *Plodia*. (*A*) Screenshot of select CUT&RUN and ATAC-seq tracks for a representative genomic locus on Chr 29. Each track represents merged views of two to four biological replicates. (*B*, *left*) Eight-state ChromHMM model emission values; darker blue indicates a higher likelihood of finding that mark in that state. (*Right*) Heat map showing enrichment for specific features (listed *below*) in each state; darker black indicates a higher likelihood of that feature being in that state. Columns have been divided by column-wise maximum. (*C*) Histogram showing the minimum distance of state designations (states 3, 7, and 8) from the end of a chromosome, in which the number of loci is binned using 30 kb windows. The genome was subdivided into three chromosome-sized groups, with Chr 1–10 (largest; 12.65–10.82 Mb) shown at the *top*, Chr 11–20 (10.56–8.45 Mb) shown in the *middle*, and Chr 21–30 (smallest; 8.34–3.98 Mb) shown at the *bottom*.

(Fig. 4B). State 8 was characterized by high emission probabilities for ATAC signal, H3K4me3, and H3K4me1, which are all marks of gene enhancers and promoters; thus, we classified state 8 as "ubiquitously active regulatory elements" (meaning active in all cell types in the testes). State 7 was enriched for ATAC signal, H3K4me3, and H3K4me1 in addition to Pol II Ser5P, H3K27ac, and H4K16ac (marks of active promoters and active transcription), and thus, we classified state 7 as "ubiquitously active TSS/exon 1." State 6 was enriched for marks associated with active transcription, but not active promoters, and showed increased H3K27me3, a mark associated with spatial or temporal silencing. Thus, we classified state 6 as "cell-type-specific or poised TSS/exon 1." State 5 showed enrichment for both H3K4me1 (active promoters) and H3K27me3 (silencing) and was therefore classified as "cell-type-specific or poised regulatory elements." State 4 had no specific enrichment and was classified as "null" chromatin. State 3 was enriched for H3K9me2 and H3K9me3, marks of constitutive silencing and, as such, was classified as "heterochromatin." Finally, states 1 and 2 are most enriched for H4K16ac and H3K36me3, marks of active transcription, and were classified as "gene body–exon dense" and "gene body–intron dense," respectively, based on their location enrichment in the genome.

To validate these classifications, we looked at several genomic features to see which state(s) they most associated with. We found that most of the genome falls into the null/no enrichment state (Fig. 4B) in which no signal is detected. In agreement with states 5 and 6 being "cell-type-specific" or "poised" states, we found that germline stem cell (GSC) genes, which should only be expressed in a specific subset of cells in testes, are most enriched for states 5 and 6 (Fig. 4B). We confirmed that annotated intergenic regions of the genome are depleted from states 1 and 2 ("gene bodies"), and annotated TSSs are enriched in states 7 and 8 (Fig. 4B).

When we looked at the location of these states genome-wide, we found that only states 3 ("heterochromatin"), 7, and 8 ("ubiquitously active regulatory elements") show biases in their genomic position. State 3 is more enriched within chromosome arms, and conversely, states 7 and 8 are more enriched toward chromosome centers, especially for big chromosomes (Fig. 4B,C; Supplemental Fig. S13). Correspondingly, we found that COs are most enriched within state 3 (darker gray box) and are largely depleted from states 7 and 8 (lightest gray boxes) (Fig. 4A,B; Supplemental Fig. S13). Together, these data suggest that although chromosome arms are not necessarily gene-poor based on the current annotations for the *Plodia* genome (Supplemental Fig. S9), they are indeed more heterochromatic than chromosome centers based on our ChromHMM analysis. These findings suggest that closed chromatin may be more permissive for CO formation in *Plodia*.

Altogether, the data presented here support a model in which the pantry moth *P. interpunctella* harbors robust CO assurance and interference with COs showing a general enrichment in heterochromatic regions of chromosome arms.

## Discussion

CO designation and the impact of CO variation are notoriously difficult to study in humans and mammalian model systems, in which CO formation occurs in only a subset of cells in testes or in fetal ovaries and rearing hundreds of mice for CO mapping experiments is extremely cost prohibitive. Here, we employ the genetically tractable pantry moth, *P. interpunctella*, to investigate CO formation in a new model system with a large number of chromosomes using a high-throughput sequencing approach. We performed whole-genome sequencing to generate SNP maps for the Savannah and the bFog *Plodia* laboratory strains. Because these are not isogenic strains, we were able to capture a robust amount of "between strain" and "within strain" variants. Why so much genetic variation exists in *Plodia* is still unclear, but one possibility is that this is caused by population bottlenecks with small laboratory culturing. The amount of genetic variation in our strains contrasts with the notion that lepidopteran genomes are highly stable (Traut et al. 2023) and instead supports a model in which lepidopteran genomes rapidly evolve (Wright et al. 2024).

Consistent with previous studies in Lepidoptera, our sequencing-based approach showed that COs are present in male meiosis but absent during female meiosis in *Plodia* (Maeda 1939; Holm and Rasmussen 1980; Rasmussen and Holm 1982; Rasmussen 1986, 1987; Shipilina et al. 2022; Xiong et al. 2023). Most of these studies have suggested that SCOs are predominant in lepidopteran spermatogenesis (Kaback et al. 1992; Jiggins et al. 2005; Yasukochi et al. 2006), which is also true in our data set. However, we did observe DCO and NoCO events by both sequencing and DNA FISH. It is important to note that the relatively small sample size here ($n = 73$ individuals for sequencing and 668 round spermatids from two gonads quantified by FISH) could skew the percentages of rare events such as NoCOs and DCOs.

The observation of frequent SCOs and limited NoCOs and DCOs combined with our CoC analyses suggest strong CO assurance and interference in *Plodia*. The predicted level of CO assurance in *Plodia* based on the Weinstein tetrad analysis (in which only ~5% of bivalents are predicted to lack COs) is lower than that reported for another holocentric species, *C. elegans*, in which essentially all bivalents receive a SCO. It is, instead, similar to other insects like *Drosophila*, in which chromosome arms fail to receive COs only ~10% of the time (except for Chr 4, which lacks COs entirely and instead relies on an alternative segregation mechanism) (Comeron et al. 2012; Miller et al. 2016; Saito and Colaiácovo 2017; Hawley et al. 2025).

In *Drosophila*, although it is unusual for any of the three main chromosomes to entirely lack COs, it is possible. In NoCO situations, *Drosophila* use a back-up segregation system to ensure all chromosomes are segregated equally (for review, see Hughes et al. 2018). We believe that NoCO bivalents in *Plodia* may similarly be segregated via an alternative "back-up" mechanism. We previously showed in silk moths that the synaptonemal complex persists through metaphase I in spermatogenesis, possibly helping to keep the homologs linked when COs do not form, similar to the mechanism in achiasmatic female meiosis (Xiang et al. 2024; Benner et al. 2026). In agreement with lepidopteran insects having a back-up mechanism for homolog linkage, a recent study in *Papilio* butterflies found something similar to what we observed here in *Plodia*, in which NoCOs were observed along with SCOs and DCOs (Xiong et al. 2023). These studies, combined with our data from *Plodia*, suggest that CO assurance might be more of a challenge for moths than for flies, perhaps owing to the increased number or smaller size of chromosomes in lepidopteran systems. Still, the mechanisms regulating CO assurance in systems with large numbers of chromosomes are not well understood and should be the subject of future studies.

Another difference we observed in CO regulation between *Plodia* and other invertebrates is the levels of CO interference. For example, *C. elegans* have extremely robust CO interference, with DCOs almost never being observed (Yokoo et al. 2012). Our Weinstein tetrad analysis of the *Plodia* data, on the other hand, suggests that *Plodia* could have DCOs up to 50% of the time for some chromosomes. This would indicate that levels of CO interference are not directly correlated with chromosome size between different species, as *Plodia* chromosomes are much smaller than *C. elegans* chromosomes (only ~4–13 Mb in *Plodia* compared with ~14–20 Mb in *C. elegans*). In agreement with the idea that chromosome size and CO formation are not directly linked, we also did not see a significant correlation between chromosome size and CO number within the *Plodia* genome, both for our raw $F_2$ CO numbers and the Weinstein tetrad estimates. Although our Weinstein tetrad estimates suggest that some *Plodia* chromosomes may harbor DCOs up to 50% of the time, other chromosomes of similar or even larger sizes are only predicted to get two COs 5%–10% of the time. A similar phenomenon was observed in *Papilio*, with chromosomes of similar sizes being differentially susceptible to DCOs (Xiong et al. 2023). At least in *Plodia*, this seems to be independent of the amount of heterochromatin or accessible chromatin per chromosome based on our ChromHMM analysis (Supplemental Fig. S14).

One possible explanation for the differences in CO interference not directly correlating with the chromosome size is the fact that CO interference is influenced by chromosome axis length

at pachytene (Kleckner 2006; Wang et al. 2017). Perhaps axis length does not scale proportionally with chromosome genomic size in moths and butterflies. That is to say, Chr 1, 3, and 5 may form more DCOs than Chr 2, 4, or 6 owing to longer chromosome axis length on Chr 1, 3 and 5, independent of genomic size, but this possibility has yet to be explored. Another possibility is that pairing timing might differ between these chromosomes, with "earlier pairing" chromosomes perhaps being more likely to form multiple COs. Several factors can impact the timing of pairing, including gene density and nuclear position/organization before pairing (MacQueen and Villeneuve 2001; Marshall and Fung 2016; Hockens et al. 2024).

Importantly, previous and new (this study) FISH-based quantifications of bivalent structures at metaphase I in *Plodia* spermatogenesis support these Weinstein predictions of chromosome-specific DCO biases (Supplemental Fig. S8A–C; Hockens et al. 2024). For all chromosomes examined by FISH, we observe two distinct post-CO structures at metaphase I: rod-shaped bivalents with one arm linked between the homologs and the other arm facing the spindle pole, and ring-shaped bivalents with both arms linked and the center of the chromosome facing the spindle pole (Supplemental Fig. S8; Hockens et al. 2024). We believe that rod-shaped bivalents result from a single, distal CO, whereas ring-shaped bivalents form after two distal COs. Consistent with the Weinstein estimates, we find that some chromosomes are more likely to form ring-shaped bivalents (two COs) than others of a similar size (e.g., Chr 3 and 5 show more DCO ring-shaped bivalents by FISH and also in the Weinstein estimates based on our sequencing-based mapping of COs) (Supplemental Fig. S8B,C). Still, it is also possible that these variations in predicted DCO frequency are exaggerated based on the Weinstein tetrad analysis, and they may not be biologically significant.

Although CO assurance and interference seem to differ slightly between moths and other holocentric invertebrates like *C. elegans*, we did find some similarities in CO position between *Plodia* and *C. elegans*. Specifically, in *C. elegans*, COs are also enriched in the heterochromatic chromosome arms, as we observed in *Plodia* (Barnes et al. 1995; Rockman and Kruglyak 2009; Gerstein et al. 2010; Ikegami et al. 2010; Liu et al. 2011; Lascarez-Lagunas et al. 2023). This is distinct from the placement of COs in many other systems, in which COs tend to be enriched in more open, active chromatin domains. For example, in many mammals, DSB formation is PRDM9 dependent. PRDM9 is a zinc finger DNA binding protein that binds to specific DNA motifs in which it deposits active histone marks. Therefore, COs form in active chromatin regions in mammals with PRDM9 (Baudat et al. 2010; Myers et al. 2010; Parvanov et al. 2010; Powers et al. 2016; Paigen and Petkov 2018). In yeast or mammals lacking PRDM9, DSBs and COs are biased toward other open chromatin regions like gene promoters (Pan et al. 2011). Similarly, studies in *Drosophila* have suggested that COs tend to avoid heterochromatin during oogenesis (Mehrotra and McKim 2006; Adrian et al. 2016; Hughes et al. 2018). Thus, although chromatin architecture is known to influence the CO landscape across systems, why holocentric species like *C. elegans* and *Plodia* preferentially place COs in heterochromatin is still unclear. It could have something to do with the holocentric chromosome architecture, or COs might be enriched in heterochromatin by other/secondary factors in these systems.

In nearly all systems studied to date, COs are enriched toward chromosome ends and away from chromosome centers (Haenel et al. 2018). Could it be that regardless of chromatin environment at chromosome ends, COs will form a minimum distance from the end of chromosomes? There are many models suggesting why such a phenomenon might be true. For example, early chromosome pairing dynamics in meiotic prophase in most systems involves telomere anchoring to the nuclear envelope and telomere-led chromosome movements (Scherthan et al. 1996; Harper et al. 2004; Naranjo and Corredor 2008; Zickler and Kleckner 2016). Similarly, synaptonemal complex assembly and DSB formation have been shown to initiate at telomere-proximal loci in several systems (Croft and Jones 1989; Lukaszewski 1997; Bass et al. 2000; Anderson and Stack 2005; Brown et al. 2005; Viera et al. 2009; Higgins et al. 2014; Klutstein and Cooper 2014; Pratto et al. 2014; Xiang et al. 2014). Together, these telomeric "head starts" to pairing and synapsis could explain why CO repair might also be more likely near telomeres (Scherthan et al. 1996; Zickler and Kleckner 2016).

In summary, this study suggests an evolutionary conservation of the meiotic CO landscape between divergent holocentric species while at the same time revealing unique evolutionary signatures of the *Plodia* genome. How COs become restricted to chromosome arms in different holocentric systems is unknown, and the role that a "centromere effect" may have on CO formation in holocentric lineages is still unclear. One unique aspect of *Plodia* CO formation compared with other previously studied holocentric species is the large number of chromosomes in *Plodia*. There is generally a lack of information on mechanisms of CO assurance in species with large numbers of chromosomes, like moths and mammals. Thus, future studies interrogating mechanisms of CO assurance and designation in *Plodia* will be critical for progress in understanding CO assurance and for addressing the impact that rapid genome evolution can have on the CO landscape.

The strong CO assurance and interference observed here establish *Plodia* as a powerful model for more directed molecular studies on CO mechanisms in systems with large numbers of chromosomes in the future. Finally, uncovering CO distributions and the genetic architecture of CO variation in a new system, as we have done here, will provide key information for researchers studying the links between genetic diversity, fertility, and disease.

## Methods

### *Plodia* strains

Two nonisogenic *P. interpunctella* strains, Savannah (assembly data at NCBI Genomes database [https://www.ncbi.nlm.nih.gov/home/genomes/] under accession number GCF_027563975.2) and bFog (sequence data at NCBI Genomes BioProject database [https://www.ncbi.nlm.nih.gov/bioproject/] under accession number PRJNA610057), were obtained from the USDA Agricultural Research Services (Savannah, Georgia, isolate, inbred since the 1960s) and The George Washington University (Dundee-Florida hybrid, inbred since 2020), respectively. Both strains were maintained on modified *Plodia* artificial diet (44% w/v coarse wheat bran, 5% Brewer's yeast flakes, 9% *d*-glucose, 30% glycerol, 3% canola oil, and 10% water) with 8 h light/16 h dark photoperiod and 60%–80% controlled humidity at 28°C. These strains were used for crosses to generate $F_1$ and $F_2$ hybrids.

### Crosses

*Plodia* WT Savannah and bFog strains were synchronized as pupae in corrugated cardboard "hotels" and sorted by sex. Virgin adults between 1 and 3 days after eclosion were then mated in a 1.25 oz plastic souffle cup (Solo) containing a pinch of diet (~0.2g) and

~1 $cm^2$ of Kimwipe to generate heterozygous $F_1$ hybrids. These crosses were performed in both directions: (1) WT Savannah males crossed to WT bFog females and (2) WT bFog males crossed to WT Savannah females. To analyze the heterozygous loci resulting from COs generated in the $F_1$ male testes, the $F_1$ hybrid males were then backcrossed to WT Savannah female or WT bFog females to produce $F_2$ offspring for downstream sequencing and CO analyses, labeled as "HS" and "HB," respectively. To avoid capturing additional COs from $F_2$ testes in our sequencing data, all $F_2$s that were sequenced were either females or males with testes removed. All $F_1$ and $F_2$ crosses were reared at room temperature (~25°C) with ambient humidity (20%–40%).

### PacBio and Illumina whole-genome sequencing

Detailed methods for whole-genome sequencing and analyses can be found in the Supplemental Methods. Briefly, PacBio long-read whole-genome sequencing of both Savannah and bFog strains (three individuals per strain) was performed using DNA from three fifth instar Savannah female larvae and three fifth instar bFog female larvae. PacBio libraries were generated using SMRTbell prep kit 3.0 with barcoded adapters; library QC was performed; and libraries were sequenced on a PacBio Sequel IIe system. PacBio circular consensus sequence (CCS) reads were converted to FASTQ format, and reads were assembled into contigs. Assembled contigs were checked for quality and aligned to the Savannah reference genome for visual inspection. QC metrics for the PacBio draft contig assemblies of Savannah and bFog strains can be found in Supplemental Table S4. The unassembled PacBio data were analyzed for both short and structural variants as described in the Supplemental Methods.

Illumina whole-genome sequencing was performed on three WT bFog and three WT Savannah female larvae, as well as 10 $F_1$ hybrid females and 83 $F_2$ hybrids (73 females, 10 males with gonads removed), for haplotype mapping and for looking for COs. Briefly, fifth instar larvae were thoroughly pulverized in a tube on dry ice using a pestle. Genomic DNA was extracted and used for generating Illumina libraries using DNA prep kit (Illumina) according to the manufacturer's protocol. Library QC was performed, and libraries were sequenced on an Illumina NovaSeq 6000 with SP200 flow cell (100 bp paired-end). Illumina data were analyzed for short variants as described below.

### ATAC-seq, RNA-seq, and CUT&RUN library generation and sequencing

Detailed methods for library preparation and sequencing can be found in the Supplemental Methods. Briefly, testes for ATAC-seq (Buenrostro et al. 2015) were dissected from fifth instar WT bFog male larvae, homogenized, strained, and cells were counted. A total of ~100,000 cells per replicate were used for tagmentation using the Active Motif ATAC-seq Kit (catalog 53150). Libraries were sequenced on an Illumina NovaSeq 6000 with SP100 flow cell (50 bp paired-end). Raw data can be accessed from NCBI (see Data access).

For RNA-seq, testes were dissected from fifth instar WT bFog larvae in ice-cold PBS. Total RNA was isolated using the RNeasy plus kit (Qiagen). Samples were purified and barcoded using TruSeq stranded mRNA library prep kit (Illumina). All libraries were pooled and sequenced on an Illumina NovaSeq 6000 with SP200 flow cell (100 bp paired-end).

For CUT&RUN (Skene and Henikoff 2017), cells were isolated from fifth instar WT bFog larval testes and pulverized with a pestle in a 1.5 mL tube. About 500,000 cells were harvested per reaction. CUT&RUN was performed using the CUTANA ChIC/CUT&RUN kit (EpiCypher) following the manufacturer's protocol. CUT&RUN libraries were generated using NEBNext Ultra II DNA library prep kit for Illumina (New England Biolabs). Libraries were sequenced on an Illumina NovaSeq 6000 with SP100 flow cell (50 bp paired-end). A complete list of antibodies used for CUT&RUN can be found in Supplemental Table S5. Detailed ATAC-seq, RNA-seq, and CUT&RUN analyses methods can be found in the Supplemental Methods.

### Downstream analysis of variants from whole-genome sequencing data

Downstream analysis of the Illumina short variants involved generating coverage tracks and colored variant tracks for $F_2$ hybrids. First, Illumina short variants, PacBio short variants, and PacBio structural variants ("union") were combined for both WT Savannah and WT bFog individuals to define the largest possible set of variants ("complete") observed in each strain. Next, for each $F_2$ "HS" hybrid, all Savannah "complete" variants were removed, and only variants that also appeared in the bFog "complete" variant set were kept. This translates to the set operation: ($F_2$–"Savannah complete") ∩ "bFog complete." For each $F_2$ "HB" hybrid, the reciprocal operation was performed: ($F_2$–"bFog complete") ∩ "Savannah complete." Finally, the remaining variants were binned in 200 bp windows across the genome to generate coverage tracks. Note that WT variants were not filtered by any criteria to cast the widest possible net of potential variant sites, whereas the $F_2$ variants were only subjected to a minimal depth filter (minimum depth ≥ 10 reads).

Coverage tracks for $F_2$ "HB" hybrids were very sparse, owing to the large number of differences from the Savannah reference genome across most chromosomes. To address this, an alternate visualization was generated as follows: Genotypes of variants observed in $F_2$ "HB" hybrids were compared directly with WT Savannah and WT bFog parents and classified into four groups: "Savannah-like," "bFog-like," "het," or "unknown." An $F_2$ variant was classified as "unknown" if variants in WT parents were (1) multiallelic, (2) identical to the $F_2$ variant (uninformative sites), or (3) absent or unknown (genotype "./.") in WT parents. If the $F_2$ variant exactly matched the Savannah or bFog parent, it was classified as "Savannah-like" or "bFog-like," respectively. Finally, any remaining variant with a heterozygous genotype was classified as "het." For visualization purposes, adjacent identical calls within 200 bp were merged together.

Any loci in which a single individual differed from the other individuals in the strain were classified as "intrastrain" variants. Loci that were nonvariant within each strain (all three individuals had the same allele) but differed between strains were classified as "interstrain" variants and were further used for haplotype generation and Oligopaints design.

The resolution for mapping COs from our data was calculated using the following procedure. First, all $F_2$ variants classified as "unknown" were removed; for "HS" and "HFS" backcrosses, regions of intrastrain variation were removed. Next, the distance between adjacent calls for each chromosome was calculated, and the median was computed. Finally, the median distances were aggregated across all individuals to obtain a population estimate. This procedure yielded the following resolution estimates for each cross: "HS," 53–72 bp; "HB," 54–76 bp; and "HFS," 57–62 bp. Skewness of variant distributions near chromosome ends within chromosome length bins for Savannah and bFog was calculated using the "skewness" function from the "e1071" R package (R Core Team 2024).

### TE and satellite repeat identification and analysis

De novo identification of TEs and other repeats in the *P. interpunctella* genome was performed using the RepeatModeler v2.0.1 tool (with -pa 8 -LTRStruct settings, and using rmblast 2.10.0+ search engine) (Flynn et al. 2020) independently on the reference assembly (ilPloInte3.2, GCF_027563975.2) and on each of the two strain-specific PacBio contig assemblies produced in this study (WT bFog and WT Savannah). The repeat library resulting from the modeling based on the reference assembly was used to annotate TEs and other repeats in the reference genome using RepeatMasker v4.1.9 (with sensitive mode and rmblastn version 2.14.1+) (Smit et al. 2013). This annotation was used for all downstream analysis of repeats, with the only exception of satellite sequences. Graphical representation of TE abundance by class was performed using the R package ggplot2 (Wickham 2016).

Satellite consensus sequences were identified only in the repeat libraries obtained from the repeat modeling on strain-specific PacBio contig assemblies. Satellite consensus sequences were subsequently annotated in the reference assembly using either the bFog or the Savannah repeat library.

Alignment of the bFog and Savannah satellite consensus sequences was performed using Clustal Omega (Sievers et al. 2011) with default settings. The intersect command in BEDTools (-wao option) (Quinlan and Hall 2010) was used to identify overlap of satellite repeats annotated in the reference assembly using the consensus sequences obtained with either the bFog or Savannah repeat library. Venn diagram was plotted using the R package eulerr v7.0.2 (https://github.com/jolars/eulerr).

To compare TE and CO density on chromosome arms (first and last third of each chromosome) versus center (middle third of each chromosome), an analysis was performed similarly to that described previously (Teterina et al. 2020). Briefly, density of TEs and COs over the reference genome was calculated using the BEDTools coverage command (100 kb windows). The Cohen's d effect size test was performed to measure positional effect of TEs and COs distribution on chromosome arms versus center using the R package lsr v0.5.2 (https://learningstatisticswithr.com/), and statistical differences were calculated using the Wilcoxon rank-sum test in base R.

To test the enrichment of COs, bFog variants, and Savannah variants over TEs, a permutation test using 1000 permutations was performed for each TE class using the overlapPermTest function of the regioneR package with default settings (Gel et al. 2016). Ideogram plots were generated using the karyoploteR package (Gel and Serra 2017).

### CO quantification and Weinstein tetrad analysis

CO positions were manually determined using coverage tracks (as shown in Fig. 2B; Supplemental Fig. S5B–E) or variant tracks (Supplemental Fig. S6A,B). Coverage tracks were used for WT Savannah backcrosses (HS) and variant tracks were used for WT bFog backcrosses (HB). To determine the approximate CO site(s) on each chromosome for each $F_2$ individual, changes in heterozygosity status were determined to the closest base pair position between identifiable strain-specific variants. Skewness of CO distributions in chromosome length bins was calculated using the function "skewness" from the "moments" R package (R Core Team 2024). Coverage tracks and variant tracks were viewed in Integrative Genomics Viewer (IGV) (Thorvaldsdóttir et al. 2013). Chromosomes were examined on the whole-chromosome scale for changes in variant or heterozygosity patterns. For coverage tracks, CO site was determined by zooming into the base pair position at which bFog variants become present/absent on the chromosomes. For variant tracks, CO site was determined by zooming into the base pair position at which heterozygous genotypes become present/absent on the chromosomes. Three to five genomes from each cross were also analyzed by a second scorer, with identical results. Weinstein tetrad analysis was performed as previously described, using a public-facing web app (Hawley et al. 2025).

### ChromHMM analysis

Detailed methods for ChromHMM analysis can be found in the Supplemental Methods. Briefly, CUT&RUN BAM files were merged with SAMtools merge (v1.22.1) (Danecek et al. 2021) to BED with BEDTools bamtobed (v2.3.1) (Quinlan and Hall 2010) and binarized with ChromHMM BinarizeBed (v1.27) (Ernst and Kellis 2017) using the default bin size. Models were trained using these binarized BED files as input to ChromHMM LearnModel. The enrichment within each state and the various enrichment tracks (for description, see Supplemental Methods) were evaluated with ChromHMM OverlapEnrichment. Details on enrichment track generation can be found in the Supplemental Methods.

### CO interference calculations

CO interference was calculated based on previously published methods (Chuang and Smith 2023). A detailed version of our methodology can be found in the Supplemental Methods. Data for *Drosophila* were analyzed in the same fashion, and CO events were derived from published data (Miller et al. 2016).

### Oligopaints' design and synthesis

For the HOPs design, a slightly modified version of previously published pipelines was used (Beliveau et al. 2015; AlHaj Abed et al. 2019). Detailed methods for Oligopaints' design and synthesis can be found in Supplemental Methods.

Oligo pools were ordered from Twist Biosciences and paints were synthesized in-house as previously described, using the T7 method (Rosin et al. 2018; Nguyen and Joyce 2019).

### Oligopaints FISH and quantification

Testes squashes and downstream Oligopaints FISH were performed as previously described (Rosin et al. 2021) using testes from fifth instar *Plodia* larvae. For detailed methods, see Supplemental Methods. COs based on HOPs probes on round spermatids were quantified manually. Data were collected from two testes (two replicates), totaling 668 nuclei.

### Immunofluorescence and quantification

*Plodia* HEI10 was identified by BLAST search using the *Bombyx mori* HEI10 protein as bait (Benner et al. 2026). A HEI10 peptide (CGSELRDKFDVIQADLKPSETFKS) was synthesized, purified, and used for monospecific polyclonal antibody generation via Pacific Immunology. *Plodia* SYCP3 antibody was previously published by our laboratory (Burns et al. 2026).

Immunofluorescence with HEI10 and SYCP3 antibodies was performed on spermatocyte spreads from WT bFog males, the protocol for which was adapted from previously published protocols (Xiang et al. 2023; Horan 2025). For the detailed protocol, see Supplemental Methods.

Quantified data were collected from two biological replicates, totaling about 50 cells. Foci quantification was performed on maximum projections in ImageJ using auto thresholding and the "analyze particles" function.

### Imaging

Oligopaints on testes squashes were imaged using a Leica DMi8 widefield inverted fluorescence microscope equipped with APO 63X/1.40 CS2 oil objective (Leica), K8 CMOS monochrome camera, LED8 light source, and DAPI/FITC/CY3/CY5/CY7 filter cubes. Images were processed using Huygens Professional express deconvolution, and tiffs were created in ImageJ.

For DAPI stain on whole-mount testes and spermatocyte spread immunofluorescence, images were acquired on a Leica Stellaris 8 resonant scanning confocal with four HyD S detectors and one HyD X SP detector, as well as the SuperZ Galvo stage. Images were postprocessed with Leica Lightning superresolution software or Huygens Professional express deconvolution, and tiffs were generated in ImageJ.

## Data access

The RNA-seq and ATAC-seq data generated in this study have been submitted to the NCBI BioProject database (https://www.ncbi.nlm.nih.gov/bioproject/) under accession number PRJNA1278932. PacBio and Illumina whole-genome sequencing data generated in this study are available under accession number PRJNA1397214. CUT&RUN data generated in this study are available under accession number PRJNA1403002. The analysis code used in this study is available at GitHub (https://github.com/NICHD-BSPC/lee-2026) and as Supplemental Code.

## Competing interest statement

The authors declare no competing interests.

## Acknowledgments

We acknowledge the late Dr. Scott Hawley for his input and suggestions on the early stages of this project, and Dr. Andre Marques for discussions at the early stages of this project. We thank Dr. Christa Heryanto for assistance with *Plodia* rearing and crosses. This work utilized the computational resources of the NIH HPC Biowulf cluster (https://hpc.nih.gov). We also thank Dr. Takashi Akera, Dr. Alex Kelly, and their laboratories for helpful discussions. Finally, we thank Dr. Stacie Hughes and Dr. Michael Lichten for suggestions and critical reading of the manuscript. This research was supported by the Intramural Research Program of the National Institutes of Health (NIH). The contributions of the NIH author(s) are considered works of the U.S. government. The findings and conclusions presented in this paper are those of the authors and do not necessarily reflect the views of the NIH or the U.S. Department of Health and Human Services. Specifically, this work was funded by the Eunice Kennedy Shriver National Institute of Child Health and Human Development, NIH (ZIAHD009019 to L.F.R. and ZICHD008986 to R.K.D.; https://www.nichd.nih.gov/about/org/dir). The funders had no role in study design, data collection and analysis, decision to publish, or preparation of the manuscript.

*Author contributions*: L.S.L. was responsible for conceptualization, experimentation and methodology, data analysis, writing, and editing. A.M. was responsible for computation, code writing and optimization, data analysis, writing, and editing. L.B. was responsible for experimentation and methodology, computation, data analysis, and writing. M.B. was responsible for computation, data analysis, and writing. L.M.R. was responsible for computation and data analysis. R.K.R. was responsible for experimentation. E.S. was responsible for computation and Oligopaints design. R.K.D. was responsible for bioinformatic conceptualization, code writing and optimization, data analysis, writing, editing, and supervision. L.F.R. was responsible for conceptualization, Oligopaints design, data analysis, writing, editing, and supervision.

## References

Adrian AB, Corchado JC, Comeron JM. 2016. Predictive models of recombination rate variation across the *Drosophila melanogaster* genome. *Genome Biol Evol* **8:** 2597–2612. doi:10.1093/gbe/evw181

AlHaj Abed J, Erceg J, Goloborodko A, Nguyen SC, McCole RB, Saylor W, Fudenberg G, Lajoie BR, Dekker J, Mirny LA, et al. 2019. Highly structured homolog pairing reflects functional organization of the *Drosophila* genome. *Nat Commun* **10:** 4485. doi:10.1038/s41467-019-12208-3

Anderson LK, Stack SM. 2005. Recombination nodules in plants. *Cytogenet Genome Res* **109:** 198–204. doi:10.1159/000082400

Arter M, Keeney S. 2024. Divergence and conservation of the meiotic recombination machinery. *Nat Rev Genet* **25:** 309–325. doi:10.1038/s41576-023-00669-8

Baril T, Hayward A. 2022. Migrators within migrators: exploring transposable element dynamics in the monarch butterfly, *Danaus plexippus*. *Mob DNA* **13:** 5. doi:10.1186/s13100-022-00263-5

Barnes TM, Kohara Y, Coulson A, Hekimi S. 1995. Meiotic recombination, noncoding DNA and genomic organization in *Caenorhabditis elegans*. *Genetics* **141:** 159–179. doi:10.1093/genetics/141.1.159

Bass HW, Riera-Lizarazu O, Ananiev EV, Bordoli SJ, Rines HW, Phillips RL, Sedat JW, Agard DA, Cande WZ. 2000. Evidence for the coincident initiation of homolog pairing and synapsis during the telomere-clustering (bouquet) stage of meiotic prophase. *J Cell Sci* **113:** 1033–1042. doi:10.1242/jcs.113.6.1033

Baudat F, Buard J, Grey C, Fledel-Alon A, Ober C, Przeworski M, Coop G, de Massy B. 2010. PRDM9 is a major determinant of meiotic recombination hotspots in humans and mice. *Science* **327:** 836–840. doi:10.1126/science.1183439

Beliveau BJ, Boettiger AN, Avendaño MS, Jungmann R, McCole RB, Joyce EF, Kim-Kiselak C, Bantignies F, Fonseka CY, Erceg J, et al. 2015. Single-molecule super-resolution imaging of chromosomes and *in situ* haplotype visualization using Oligopaint FISH probes. *Nat Commun* **6:** 7147. doi:10.1038/ncomms8147

Benner L, Richmond M, Xiang Y, Lee L, Hockens CB, Li T, Yu Z, Tsuchiya D, Huang S, Tromer EC, et al. 2026. Programmed meiotic errors facilitate dichotomous sperm production in the silkworm, *Bombyx mori*. *Proc Natl Acad Sci* **123:** e2520991123. doi:10.1073/pnas.2520991123

Bolcun-Filas E, Handel MA. 2018. Meiosis: the chromosomal foundation of reproduction. *Biol Reprod* **99:** 112–126. doi:10.1093/biolre/ioy021

Bomblies K, Higgins JD, Yant L. 2015. Meiosis evolves: adaptation to external and internal environments. *New Phytol* **208:** 306–323. doi:10.1111/nph.13499

Brekke C, Johnston SE, Knutsen TM, Berg P. 2023. Genetic architecture of individual meiotic crossover rate and distribution in Atlantic Salmon. *Sci Rep* **13:** 20481. doi:10.1038/s41598-023-47208-3

Brown PW, Judis L, Chan ER, Schwartz S, Seftel A, Thomas A, Hassold TJ. 2005. Meiotic synapsis proceeds from a limited number of subtelomeric sites in the human male. *Am J Hum Genet* **77:** 556–566. doi:10.1086/468188

Buenrostro J, Wu B, Chang H, Greenleaf W. 2015. ATAC-seq: a method for assaying chromatin accessibility genome-wide. *Curr Protoc Mol Biol* **109:** 21.29.1–21.29.9. doi:10.1002/0471142727.mb2129s109

Burns EE, Amoiroglou A, Fagerstrom CJ, Ryniawec JM, Lee L, Runyan RK, Rosin LF, Rogers GC, Rusan NM. 2026. Visualizing *Drosophila* centrioles by expansion microscopy. *J Cell Sci* **139:** jcs264338. doi:10.1242/jcs.264338

Castellani M, Zhang M, Thangavel G, Mata-Sucre Y, Lux T, Campoy JA, Marek M, Huettel B, Sun H, Mayer KFX, et al. 2024. Meiotic recombination dynamics in plants with repeat-based holocentromeres shed light on the primary drivers of crossover patterning. *Nat Plants* **10:** 423–438. doi:10.1038/s41477-024-01625-y

Chuang Y-C, Smith GR. 2023. Meiotic crossover interference: methods of analysis and mechanisms of action. *Curr Top Dev Biol* **151:** 217–244. doi:10.1016/bs.ctdb.2022.04.006

Comeron JM, Ratnappan R, Bailin S. 2012. The many landscapes of recombination in *Drosophila melanogaster*. *PLoS Genet* **8:** e1002905. doi:10.1371/journal.pgen.1002905

Croft JA, Jones GH. 1989. Meiosis in Mesostoma ehrenbergii ehrenbergii. IV. Recombination nodules in spermatocytes and a test of the correspondence of late recombination nodules and chiasmata. *Genetics* **121:** 255–262. doi:10.1093/genetics/121.2.255

Danecek P, Bonfield JK, Liddle J, Marshall J, Ohan V, Pollard MO, Whitwham A, Keane T, McCarthy SA, Davies RM, et al. 2021. Twelve

years of SAMtools and BCFtools. *GigaScience* **10:** giab008. doi:10.1093/gigascience/giab008
Dapper AL, Payseur BA. 2019. Molecular evolution of the meiotic recombination pathway in mammals. *Evolution* **73:** 2368–2389. doi:10.1111/evo.13850
Darlington CD, Dark SOS. 1932. The origin and behaviour of chiasmata, II: *Senobothrus parallelus*. *Cytologia (Tokyo)* **3:** 169–185. doi:10.1508/cytologia.3.169
Davis L, Smith GR. 2003. Nonrandom homolog segregation at meiosis I in *Schizosaccharomyces pombe* mutants lacking recombination. *Genetics* **163:** 857–874. doi:10.1093/genetics/163.3.857
de Massy B. 2013. Initiation of meiotic recombination: how and where? Conservation and specificities among eukaryotes. *Annu Rev Genet* **47:** 563–599. doi:10.1146/annurev-genet-110711-155423
Ernst J, Kellis M. 2012. ChromHMM: automating chromatin-state discovery and characterization. *Nat Methods* **9:** 215–216. doi:10.1038/nmeth.1906
Ernst J, Kellis M. 2017. Chromatin-state discovery and genome annotation with ChromHMM. *Nat Protoc* **12:** 2478–2492. doi:10.1038/nprot.2017.124
Eyre-Walker A. 1993. Recombination and mammalian genome evolution. *Proc Biol Sci* **252:** 237–243. doi:10.1098/rspb.1993.0071
Finnegan DJ. 1989. Eukaryotic transposable elements and genome evolution. *Trends Genet* **5:** 103–107. doi:10.1016/0168-9525(89)90039-5
Flynn JM, Hubley R, Goubert C, Rosen J, Clark AG, Feschotte C, Smit AF. 2020. Repeatmodeler2 for automated genomic discovery of transposable element families. *Proc Natl Acad Sci* **117:** 9451–9457. doi:10.1073/pnas.1921046117
Foss E, Lande R, Stahl FW, Steinberg CM. 1993. Chiasma interference as a function of genetic distance. *Genetics* **133:** 681–691. doi:10.1093/genetics/133.3.681
Gbadegesin MA. 2012. Transposable elements in the genomes: parasites, junks or drivers of evolution? *Afr J Med Med Sci* **41 Suppl:** 13–25.
Gel B, Serra E. 2017. karyoploteR: an R/Bioconductor package to plot customizable genomes displaying arbitrary data. *Bioinformatics* **33:** 3088–3090. doi:10.1093/bioinformatics/btx346
Gel B, Díez-Villanueva A, Serra E, Buschbeck M, Peinado MA, Malinverni R. 2016. regioneR: an R/Bioconductor package for the association analysis of genomic regions based on permutation tests. *Bioinformatics* **32:** 289–291. doi:10.1093/bioinformatics/btv562
Gerstein MB, Lu ZJ, Van Nostrand EL, Cheng C, Arshinoff BI, Liu T, Yip KY, Robilotto R, Rechtsteiner A, Ikegami K, et al. 2010. Integrative analysis of the *Caenorhabditis elegans* genome by the modENCODE project. *Science* **330:** 1775–1787. doi:10.1126/science.1196914
Gerton JL, Hawley RS. 2005. Homologous chromosome interactions in meiosis: diversity amidst conservation. *Nat Rev Genet* **6:** 477–487. doi:10.1038/nrg1614
Glémin S, Clément Y, David J, Ressayre A. 2014. GC content evolution in coding regions of angiosperm genomes: a unifying hypothesis. *Trends Genet* **30:** 263–270. doi:10.1016/j.tig.2014.05.002
Gray S, Cohen PE. 2016. Control of meiotic crossovers: from double-strand break formation to designation. *Annu Rev Genet* **50:** 175–210. doi:10.1146/annurev-genet-120215-035111
Haenel Q, Laurentino TG, Roesti M, Berner D. 2018. Meta-analysis of chromosome-scale crossover rate variation in eukaryotes and its significance to evolutionary genomics. *Mol Ecol* **27:** 2477–2497. doi:10.1111/mec.14699
Harper L, Golubovskaya I, Cande WZ. 2004. A bouquet of chromosomes. *J Cell Sci* **117:** 4025–4032. doi:10.1242/jcs.01363
Hawley RS, Price A, Li H, Jagannathan M, Staber C, Hughes SE, Williams S, Perera A, Egidy RR, Lawlor A, et al. 2025. Patterns of crossover distribution in *Drosophila mauritiana* necessitate a re-thinking of the centromere effect on crossing over. *Genetics* **230:** iyaf039. doi:10.1093/genetics/iyaf039
Heryanto C, Hanly JJ, Mazo-Vargas A, Tendolkar A, Martin A. 2022. Mapping and CRISPR homology-directed repair of a recessive white eye mutation in Plodia moths. *iScience* **25:** 103885. doi:10.1016/j.isci.2022.103885
Higgins JD, Osman K, Jones GH, Franklin FCH. 2014. Factors underlying restricted crossover localization in barley meiosis. *Annu Rev Genet* **48:** 29–47. doi:10.1146/annurev-genet-120213-092509
Hinch AG, Zhang G, Becker PW, Moralli D, Hinch R, Davies B, Bowden R, Donnelly P. 2019. Factors influencing meiotic recombination revealed by whole-genome sequencing of single sperm. *Science* **363:** eaau8861. doi:10.1126/science.aau8861
Hockens C, Lorenzi H, Wang TT, Lei EP, Rosin LF. 2024. Chromosome segregation during spermatogenesis occurs through a unique center-kinetic mechanism in holocentric moth species. *PLoS Genet* **20:** e1011329. doi:10.1371/journal.pgen.1011329
Holm PB, Rasmussen SW. 1980. Chromosome pairing, recombination nodules and chiasma formation in diploid Bombyx males. *Carlsberg Res Commun* **45:** 483–548. doi:10.1007/BF02932921
Horan TSA. 2025. Preparation of meiotic chromosome spreads from mouse oocytes for assessment of synapsis and recombination. *J Vis Exp* (221). doi:10.3791/68749
Hughes SE, Miller DE, Miller AL, Hawley RS. 2018. Female meiosis: synapsis, recombination, and segregation in *Drosophila melanogaster*. *Genetics* **208:** 875–908. doi:10.1534/genetics.117.300081
Ikegami K, Egelhofer TA, Strome S, Lieb JD. 2010. *Caenorhabditis elegans* chromosome arms are anchored to the nuclear membrane via discontinuous association with LEM-2. *Genome Biol* **11:** R120. doi:10.1186/gb-2010-11-12-r120
Jiggins CD, Mavarez J, Beltrán M, McMillan WO, Johnston JS, Bermingham E. 2005. A genetic linkage map of the mimetic butterfly *Heliconius melpomene*. *Genetics* **171:** 557–570. doi:10.1534/genetics.104.034686
Kaback DB, Guacci V, Barber D, Mahon JW. 1992. Chromosome size-dependent control of meiotic recombination. *Science* **256:** 228–232. doi:10.1126/science.1566070
Keeney S, Lange J, Mohibullah N. 2014. Self-organization of meiotic recombination initiation: general principles and molecular pathways. *Annu Rev Genet* **48:** 187–214. doi:10.1146/annurev-genet-120213-092304
Kleckner N. 2006. Chiasma formation: chromatin/axis interplay and the role(s) of the synaptonemal complex. *Chromosoma* **115:** 175–194. doi:10.1007/s00412-006-0055-7
Klutstein M, Cooper JP. 2014. The chromosomal courtship dance-homolog pairing in early meiosis. *Curr Opin Cell Biol* **26:** 123–131. doi:10.1016/j.ceb.2013.12.004
Kong A, Thorleifsson G, Frigge ML, Masson G, Gudbjartsson DF, Villemoes R, Magnusdottir E, Olafsdottir SB, Thorsteinsdottir U, Stefansson K. 2014. Common and low-frequency variants associated with genome-wide recombination rate. *Nat Genet* **46:** 11–16. doi:10.1038/ng.2833
Kumar R, Bourbon H-M, de Massy B. 2010. Functional conservation of Mei4 for meiotic DNA double-strand break formation from yeasts to mice. *Genes Dev* **24:** 1266–1280. doi:10.1101/gad.571710
Lascarez-Lagunas LI, Martinez-Garcia M, Nadarajan S, Diaz-Pacheco BN, Berson E, Colaiácovo MP. 2023. Chromatin landscape, DSB levels, and cKU-70/80 contribute to patterning of meiotic DSB processing along chromosomes in *C. elegans*. *PLoS Genet* **19:** e1010627. doi:10.1371/journal.pgen.1010627
Lawlor MA, Ellison CE. 2023. Evolutionary dynamics between transposable elements and their host genomes: mechanisms of suppression and escape. *Curr Opin Genet Dev* **82:** 102092. doi:10.1016/j.gde.2023.102092
Lenormand T, Dutheil J. 2005. Recombination difference between sexes: a role for haploid selection. *PLoS Biol* **3:** e63. doi:10.1371/journal.pbio.0030063
Liu T, Rechtsteiner A, Egelhofer TA, Vielle A, Latorre I, Cheung M-S, Ercan S, Ikegami K, Jensen M, Kolasinska-Zwierz P, et al. 2011. Broad chromosomal domains of histone modification patterns in *C. elegans*. *Genome Res* **21:** 227–236. doi:10.1101/gr.115519.110
Lukaszewski AJ. 1997. The development and meiotic behavior of asymmetrical isochromosomes in wheat. *Genetics* **145:** 1155–1160. doi:10.1093/genetics/145.4.1155
Lum PTM, Flaherty BR. 1970. Regulating oviposition by *Plodia interpunctella1* in the laboratory by light and dark conditions. *J Econ Entomol* **63:** 236–239. doi:10.1093/jee/63.1.236
MacQueen AJ, Villeneuve AM. 2001. Nuclear reorganization and homologous chromosome pairing during meiotic prophase require *C. elegans chk-2*. *Genes Dev* **15:** 1674–1687. doi:10.1101/gad.902601
Maeda T. 1939. Chiasma studies in the silkworm, *Bombyx mori* L. *Japanese J Genet* **15:** 118–127. doi:10.1266/jjg.15.118
Marshall WF, Fung JC. 2016. Modeling meiotic chromosome pairing: nuclear envelope attachment, telomere-led active random motion, and anomalous diffusion. *Phys Biol* **13:** 026003. doi:10.1088/1478-3975/13/2/026003
Martin RH. 2006. Meiotic chromosome abnormalities in human spermatogenesis. *Reprod Toxicol* **22:** 142–147. doi:10.1016/j.reprotox.2006.03.013
Mehrotra S, McKim KS. 2006. Temporal analysis of meiotic DNA double-strand break formation and repair in *Drosophila* females. *PLoS Genet* **2:** e200. doi:10.1371/journal.pgen.0020200
Miller DE, Smith CB, Kazemi NY, Cockrell AJ, Arvanitakis AV, Blumenstiel JP, Jaspersen SL, Hawley RS. 2016. Whole-genome analysis of individual meiotic events in *Drosophila melanogaster* reveals that noncrossover gene conversions are insensitive to interference and the centromere effect. *Genetics* **203:** 159–171. doi:10.1534/genetics.115.186486
Muller HJ. 1916. The mechanism of crossing-over. *Am Nat* **50:** 193–221. doi:10.1086/279534
Myers S, Bowden R, Tumian A, Bontrop RE, Freeman C, MacFie TS, McVean G, Donnelly P. 2010. Drive against hotspot motifs in primates

implicates the *PRDM9* gene in meiotic recombination. *Science* **327:** 876–879. doi:10.1126/science.1182363
Nambiar M, Chuang Y-C, Smith GR. 2019. Distributing meiotic crossovers for optimal fertility and evolution. *DNA Repair (Amst)* **81:** 102648. doi:10.1016/j.dnarep.2019.102648
Naranjo T, Corredor E. 2008. Nuclear architecture and chromosome dynamics in the search of the pairing partner in meiosis in plants. *Cytogenet Genome Res* **120:** 320–330. doi:10.1159/000121081
Nguyen SC, Joyce EF. 2019. Programmable chromosome painting with Oligopaints. *Methods Mol Biol* **2038:** 167–180. doi:10.1007/978-1-4939-9674-2_11
Nicklas RB. 1997. How cells get the right chromosomes. *Science* **275:** 632–637. doi:10.1126/science.275.5300.632
Okazaki S, Tsuchida K, Maekawa H, Ishikawa H, Fujiwara H. 1993. Identification of a pentanucleotide telomeric sequence, (TTAGG)n, in the silkworm *Bombyx mori* and in other insects. *Mol Cell Biol* **13:** 1424–1432. doi:10.1128/mcb.13.3.1424-1432.1993
Otto SP, Payseur BA. 2019. Crossover interference: shedding light on the evolution of recombination. *Annu Rev Genet* **53:** 19–44. doi:10.1146/annurev-genet-040119-093957
Owen ARG. 1949. A possible interpretation of the apparent interference across the centromere found by Callan and Montalenti *in Culex pipiens*. *Heredity (Edinb)* **3:** 357–367. doi:10.1038/hdy.1949.26
Paigen K, Petkov PM. 2018. PRDM9 and its role in genetic recombination. *Trends Genet* **34:** 291–300. doi:10.1016/j.tig.2017.12.017
Pan J, Sasaki M, Kniewel R, Murakami H, Blitzblau HG, Tischfield SE, Zhu X, Neale MJ, Jasin M, Socci ND, et al. 2011. A hierarchical combination of factors shapes the genome-wide topography of yeast meiotic recombination initiation. *Cell* **144:** 719–731. doi:10.1016/j.cell.2011.02.009
Parvanov ED, Petkov PM, Paigen K. 2010. *Prdm9* controls activation of mammalian recombination hotspots. *Science* **327:** 835. doi:10.1126/science.1181495
Pazhayam NM, Turcotte CA, Sekelsky J. 2021. Meiotic crossover patterning. *Front Cell Dev Biol* **9:** 681123. doi:10.3389/fcell.2021.681123
Perrier C, Allio R, Legeai F, Gautier M, Bénéluz F, Marande W, Theron A, Rodde N, Herrera M, Sauné L, et al. 2025. Transposable element accumulation drives genome size increase in *Hylesia metabus* (Lepidoptera: Saturniidae), an urticating moth species from South America. *J Hered* **116:** 344–353. doi:10.1093/jhered/esae069
Powers NR, Parvanov ED, Baker CL, Walker M, Petkov PM, Paigen K. 2016. The meiotic recombination activator PRDM9 trimethylates both H3K36 and H3K4 at recombination hotspots *in vivo*. *PLoS Genet* **12:** e1006146. doi:10.1371/journal.pgen.1006146
Pratto F, Brick K, Khil P, Smagulova F, Petukhova GV, Camerini-Otero RD. 2014. DNA recombination. Recombination initiation maps of individual human genomes. *Science* **346:** 1256442. doi:10.1126/science.1256442
Price DJ, Bantock CR. 1975. Marginal populations of *Cepaea nemoralis* (L.) on the Brendon Hills, England. II. Variation in chiasma frequency. *Evolution* **29:** 278–286. doi:10.1111/j.1558-5646.1975.tb00208.x
Quinlan AR, Hall IM. 2010. BEDTools: a flexible suite of utilities for comparing genomic features. *Bioinformatics* **26:** 841–842. doi:10.1093/bioinformatics/btq033
Rasmussen SW. 1977. Meiosis in *Bombyx mori* females. *Philos Trans R Soc Lond B Biol Sci* **277:** 343–350. doi:10.1098/rstb.1977.0022
Rasmussen SW. 1986. Initiation of synapsis and interlocking of chromosomes during zygotene in *Bombyx* spermatocytes. *Carlsberg Res Commun* **51:** 401–432. doi:10.1007/BF02907315
Rasmussen SW. 1987. Chromosome pairing in autotetraploid Bombyx males: inhibition of multivalent correction by crossing over. *Carlsberg Res Commun* **52:** 211–242. doi:10.1007/BF02910593
Rasmussen SW, Holm PB. 1982. The meiotic prophase in *Bombyx mori*. In *Insect ultrastructure* (ed. King RC, Akai H), Vol. 1, pp. 61–85. Springer US, Boston, MA.
R Core Team. 2024. *R: a language and environment for statistical computing*. R Foundation for Statistical Computing, Vienna. https://www.R-project.org/.
Rockman MV, Kruglyak L. 2009. Recombinational landscape and population genomics of *Caenorhabditis elegans*. *PLoS Genet* **5:** e1000419. doi:10.1371/journal.pgen.1000419
Rodgers-Melnick E, Bradbury PJ, Elshire RJ, Glaubitz JC, Acharya CB, Mitchell SE, Li C, Li Y, Buckler ES. 2015. Recombination in diverse maize is stable, predictable, and associated with genetic load. *Proc Natl Acad Sci* **112:** 3823–3828. doi:10.1073/pnas.1413864112
Rosin LF, Nguyen SC, Joyce EF. 2018. Condensin II drives large-scale folding and spatial partitioning of interphase chromosomes in *Drosophila* nuclei. *PLoS Genet* **14:** e1007393. doi:10.1371/journal.pgen.1007393
Rosin LF, Gil J Jr, Drinnenberg IA, Lei EP. 2021. Oligopaint DNA FISH reveals telomere-based meiotic pairing dynamics in the silkworm, *Bombyx mori*. *PLoS Genet* **17:** e1009700. doi:10.1371/journal.pgen.1009700
Rybnikov SR, Frenkel Z, Hübner S, Weissman DB, Korol AB. 2023. Modeling the evolution of recombination plasticity: a prospective review. *Bioessays* **45:** e2200237. doi:10.1002/bies.202200237
Saito TT, Colaiácovo MP. 2017. Regulation of crossover frequency and distribution during meiotic recombination. *Cold Spring Harb Symp Quant Biol* **82:** 223–234. doi:10.1101/sqb.2017.82.034132
Samuk K, Manzano-Winkler B, Ritz KR, Noor MAF. 2020. Natural selection shapes variation in genome-wide recombination rate in *Drosophila pseudoobscura*. *Curr Biol* **30:** 1517–1528.e6. doi:10.1016/j.cub.2020.03.053
Scherthan H, Weich S, Schwegler H, Heyting C, Härle M, Cremer T. 1996. Centromere and telomere movements during early meiotic prophase of mouse and man are associated with the onset of chromosome pairing. *J Cell Biol* **134:** 1109–1125. doi:10.1083/jcb.134.5.1109
Shipilina D, Näsvall K, Höök L, Vila R, Talavera G, Backström N. 2022. Linkage mapping and genome annotation give novel insights into gene family expansions and regional recombination rate variation in the painted lady (*Vanessa cardui*) butterfly. *Genomics* **114:** 110481. doi:10.1016/j.ygeno.2022.110481
Sievers F, Wilm A, Dineen D, Gibson TJ, Karplus K, Li W, Lopez R, McWilliam H, Remmert M, Söding J, et al. 2011. Fast, scalable generation of high-quality protein multiple sequence alignments using clustal omega. *Mol Syst Biol* **7:** 539. doi:10.1038/msb.2011.75
Skene PJ, Henikoff S. 2017. An efficient targeted nuclease strategy for high-resolution mapping of DNA binding sites. *eLife* **6:** e21856. doi:10.7554/eLife.21856
Smit A, Hubley R, Green P. 2013. RepeatMasker. http://www.repeatmasker.org.
Stapley J, Feulner PGD, Johnston SE, Santure AW, Smadja CM. 2017. Variation in recombination frequency and distribution across eukaryotes: patterns and processes. *Philos Trans R Soc Lond B Biol Sci* **372:** 20160455. doi:10.1098/rstb.2016.0455
Sturtevant AH. 1915. The behavior of the chromosomes as studied through linkage. *Z Indukt Abstammungs Vererbungsl* **13:** 234–287. doi:10.1007/BF01792906
Sun F, Oliver-Bonet M, Liehr T, Starke H, Ko E, Rademaker A, Martin RH. 2007a. Discontinuities and unsynapsed regions in meiotic chromosomes have a *trans* effect on meiotic recombination of some chromosomes in human males. *Cytogenet Genome Res* **119:** 27–32. doi:10.1159/000109615
Sun F, Turek P, Greene C, Ko E, Rademaker A, Martin RH. 2007b. Abnormal progression through meiosis in men with nonobstructive azoospermia. *Fertil Steril* **87:** 565–571. doi:10.1016/j.fertnstert.2006.07.1531
Teterina AA, Willis JH, Phillips PC. 2020. Chromosome-level assembly of the *Caenorhabditis remanei* genome reveals conserved patterns of nematode genome organization. *Genetics* **214:** 769–780. doi:10.1534/genetics.119.303018
Theodosiou L, McMillan WO, Puebla O. 2016. Recombination in the eggs and sperm in a simultaneously hermaphroditic vertebrate. *Proc Biol Sci* **283:** 20161821. doi:10.1098/rspb.2016.1821
Thorvaldsdóttir H, Robinson JT, Mesirov JP. 2013. Integrative Genomics Viewer (IGV): high-performance genomics data visualization and exploration. *Brief Bioinformatics* **14:** 178–192. doi:10.1093/bib/bbs017
Torres API, Höök L, Näsvall K, Shipilina D, Wiklund C, Vila R, Pruisscher P, Backström N. 2023. The fine-scale recombination rate variation and associations with genomic features in a butterfly. *Genome Res* **33:** 810–823. doi:10.1101/gr.277414.122
Traut W, Sahara K, ffrench-Constant RH. 2023. Lepidopteran Synteny Units reveal deep chromosomal conservation in butterflies and moths. *G3 (Bethesda)* **13:** jkad134. doi:10.1093/g3journal/jkad134
Viera A, Santos JL, Rufas JS. 2009. Relationship between incomplete synapsis and chiasma localization. *Chromosoma* **118:** 377–389. doi:10.1007/s00412-009-0204-x
Vítková M, Král J, Traut W, Zrzavý J, Marec F. 2005. The evolutionary origin of insect telomeric repeats, $(TTAGG)_N$. *Chromosome Res* **13:** 145–156. doi:10.1007/s10577-005-7721-0
Wang S, Hassold T, Hunt P, White MA, Zickler D, Kleckner N, Zhang L. 2017. Inefficient crossover maturation underlies elevated aneuploidy in human female meiosis. *Cell* **168:** 977–989.e17. doi:10.1016/j.cell.2017.02.002
Wang S, Shang Y, Liu Y, Zhai B, Yang X, Zhang L. 2021. Crossover patterns under meiotic chromosome program. *Asian J Androl* **23:** 562–571. doi:10.4103/aja.aja_86_20
Weinstein A. 1936. The theory of multiple-strand crossing over. *Genetics* **21:** 155–199. doi:10.1093/genetics/21.3.155
Weinstein A. 1958. The geometry and mechanics of crossing over. *Cold Spring Harb Symp Quant Biol* **23:** 177–196. doi:10.1101/SQB.1958.023.01.022
Wickham H. 2016. *ggplot2: elegant graphics for data analysis*. Springer-Verlag, New York. https://ggplot2.tidyverse.org/.
Wright CJ, Stevens L, Mackintosh A, Lawniczak M, Blaxter M. 2024. Comparative genomics reveals the dynamics of chromosome evolution

in Lepidoptera. *Nat Ecol Evol* **8:** 777–790. doi:10.1038/s41559-024-02329-4

Xiang Y, Miller DE, Ross EJ, Sánchez Alvarado A, Hawley RS. 2014. Synaptonemal complex extension from clustered telomeres mediates full-length chromosome pairing in *Schmidtea mediterranea*. *Proc Natl Acad Sci* **111:** E5159–E5168. doi:10.1073/pnas.1420287111

Xiang Y, Tsuchiya D, Guo F, Gardner J, McCroskey S, Price A, Tromer EC, Walters JR, Lake CM, Hawley RS. 2023. A molecular cell biology toolkit for the study of meiosis in the silkworm *Bombyx mori*. *G3 (Bethesda)* **13:** jkad058. doi:10.1093/g3journal/jkad058

Xiang Y, Tsuchiya D, Yu Z, Zhao X, McKinney S, Unruh J, Slaughter B, Lake CM, Hawley RS. 2024. Multiple reorganizations of the lateral elements of the synaptonemal complex facilitate homolog segregation in *Bombyx mori* oocytes. *Curr Biol* **34:** 352–360.e4. doi:10.1016/j.cub.2023.12.018

Xiong T, Tarikere S, Rosser N, Li X, Yago M, Mallet J. 2023. A polygenic explanation for Haldane's rule in butterflies. *Proc Natl Acad Sci* **120:** e2300959120. doi:10.1073/pnas.2300959120

Yasukochi Y, Ashakumary LA, Baba K, Yoshido A, Sahara K. 2006. A second-generation integrated map of the silkworm reveals synteny and conserved gene order between lepidopteran insects. *Genetics* **173:** 1319–1328. doi:10.1534/genetics.106.055541

Yokoo R, Zawadzki KA, Nabeshima K, Drake M, Arur S, Villeneuve AM. 2012. COSA-1 reveals robust homeostasis and separable licensing and reinforcement steps governing meiotic crossovers. *Cell* **149:** 75–87. doi:10.1016/j.cell.2012.01.052

Zhang C, Wang L, Dou L, Yue B, Xing J, Li J. 2023. Transposable elements shape the genome diversity and the evolution of Noctuidae species. *Genes (Basel)* **14:** 1244. doi:10.3390/genes14061244

Zickler D, Kleckner N. 2016. A few of our favorite things: pairing, the bouquet, crossover interference and evolution of meiosis. *Semin Cell Dev Biol* **54:** 135–148. doi:10.1016/j.semcdb.2016.02.024

*Received January 23, 2026; accepted in revised form June 17, 2026*.